Measuring Optomechanics with a Photon STM in the High Vacuum Environment

by

Kyle Reid

A thesis submitted in partial fulfillment of the requirements for the degree of

Master of Science

Department of Physics

University of Alberta

Abstract

Optomechanics, the sensing of mechanical movement using optical modes, has seen great advancement in recent years and has been used for its high displacement sensitivity to couple to a variety of mechanical devices. Torsional devices have historically been used for measuring de Haas-van Alphen effect, shear modulus, superfluids, superconductors, the angular momentum of light, switching of magnetic states, and other applications. Combining these two together, a silicon microdisk coupled to a torsional resonator has been observed before to have sensitivities of 4 nrad $\mathrm{Hz}^{-1/2}$ and 7 fm $\mathrm{Hz}^{-1/2}$.

A cryogenic ultra-high vacuum (UHV) system holds the possibilities of analyzing these devices at 4 K in a much higher vacuum than has been studied before. We have retrofitted a former STM with a tapered optical fiber to couple light to a silicon microdisk. This "Photon STM" (P-STM) has the potential to not only couple to optical devices, but map the optical topography of a sample by using a modified tunnel current technique. This thesis shows how the P-STM was constructed and demonstrated its ability to couple to a 38 μm diameter optical disk and measured a nearby torsional resonator in high vacuum, with sensitivities down to 200 fm $\mathrm{Hz}^{-1/2}$ and 80 nrad $\mathrm{Hz}^{-1/2}$.

To my maternal grandfather Gordan "Bumpa" Gainer,

for challenging me to continually learn, develop my character, and be thankful in all things.

"It is not the critic who counts; not the man who points out how the strong man stumbles, or where the doer of deeds could have done them better. The credit belongs to the man who is actually in the arena, whose face is marred by dust and sweat and blood; who strives valiantly; who errs, who comes short again and again, because there is no effort without error and shortcoming; but who does actually strive to do the deeds; who knows great enthusiasms, the great devotions; who spends himself in a worthy cause; who at the best knows in the end the triumph of high achievement, and who at the worst, if he fails, at least fails while daring greatly, so that his place shall never be with those cold and timid souls who neither know victory nor defeat."
- Theodore Roosevelt

Acknowledgements

The attaining of this degree over the past two and a half years is not mine only, but is my supervisors, my fellow graduate students', my family's, and my friends'. I would first like to thank my parents, for always encouraging me, making sure I was continually challenged, and supporting me in everything. Dad, for teaching me how to take apart almost every aspect of a car, teaching me the value of hard work through building something with my own hands, and handing down all of the traits he learned from his father. I will be grateful my entire life for my Mom. She devoted time inside and outside of school to ensure I was always challenged in every area, especially those I excelled at. This thesis and attaining of higher knowledge could not have been done without my grandparents. Gordan "Bumpa" Gainer and Thelma "Grandma" Gainer. Bumpa was detail oriented and always followed sound, scientific reasoning. His attaining of his doctorate at Iowa State under Professor Henry Gillman and his plethora of patents he developed while at Westing House helped me realize the reality of graduate school and the continuous seeking of higher knowledge. It has lead me to strive to never stop learning or become stagnant, but to keep pushing myself to higher levels than I could have imagined.

I would like to extend my deepest thanks to my supervisors, Professors Mark Freeman and John Davis. Both gave me this astounding opportunity to continue

my education and use the full extent of my abilities. David Fortin gave me engaging new ideas when I was stumped during fiber pulling and optical coupling,. He taught me how to engineer on a smaller scale including rewiring the STM multiple times. Professors Frank Hegmann, Al Meldrum, and Joeseph Maciejko were instrumental on completing my degree. Sarah Derr and Professor Richard Marchand helped to keep me on track to finish my thesis and schedule my defense. I am grateful for the support of Professor Isaac Isaac who has given me immense opportunities to further my teaching career. Thanks to the machinists Devin Segato, Jordan Cameron, and Paul Zimmermann for teaching me not only how to machine with a lathe and mill, but having the patience and taking the time out of their busy days to continue teaching me more refined techniques.

I greatly appreciate the help of Paul Kim and Callum Doolin of the Davis group, whose research and devices I built the P-STM and made the new fiber pulling procedure from and for helping me understand optomechanics and how to make simulations. Joe Losby was extremely helpful in understanding magnetic properties and bouncing ideas off of. Lance Parsons helped me realize the necessary timelines for developing my project and prepared me for future endeavors. Fatemeh Fani Suni provided encouragement and help both for my project and the graduate classes I took. I am very thankful to Bradley Hauer's assistance in understanding the theory of optomechanics and fiber pulling. Allison Macdonald's help was primary to understand and build the necessary optical circuits. I will always be grateful for Taleana Huff and Stephen Lane in reading my thesis and listening to my defense presentation. They helped me to keep progressing and lifted my spirits when it mattered most. Chris Polachic, Burkhard Ritter, and Jin Xu increased my understand of theoretical condensed matter physics and taught me the intricacies of LaTeX.

Contents

List of Tables

List of Figures

Chapter 1

Introduction

1.1 An Introduction to Torsional Mechanics

Torsional mechanics is the twisting of an object due to an applied torque and is one of many ways torque, force, and mass are measured. Before considering torque, Hooke's Law must be consulted, which is

$$\vec{F} = -k\vec{x}, \tag{1.1}$$

with $\vec{F}$ being the restoring force from a displacement $\vec{x}$ with a spring constant of k. This concept can be extended to torsional systems using the equation

$$\vec{\tau} = -\kappa\vec{\theta}, \tag{1.2}$$

where $\vec{\tau}$ represents torque, κ the torsional spring constant, and $\vec{\theta}$ the angular displacement.

Torsional sensors have played a major role in scientific measurement for hun-

dreds of years, one of the most notable being gravitational measurement. In 1798, Cavendish incorporated a torsion device which measured the gravitational attractive force as a torque between two different sizes of lead balls and comparing the results to their weight, thereby finding the density of the Earth [1]. Two hundred years later, a similar device was used by Luther and Towler for increased gravitational force sensing [2]. Torsional sensors have aided in greater resolution of electric charge [3] on the nanometer scale by employing a torsional paddle resonator.

Expansion of these sensors has extended to various aspects of magnetometry, including the use of nanotorsional resonators and switching of vortex states [4]. The ability to measure the Casimir force would be greatly limited if it was not for sensors such as these [5]. Torsional balances have also placed a role in measuring the de Haas-van Alphen effect [6] along with torque magnetometry down to 0.1 K [7].

Many of these devices have progressed to the nanoscale environment using various techniques, such as optical and electron beam lithography. The progression has been to continue to scale down both the size and mass of these resonators in the hopes of witnessing quantum mechanical effects with increased sensitivity. Looking at measuring physical properties, chemically etched oscillators on silicon have been used to measure the shear modulus [8]. The transition to the superfluid state in 2D ^{4}He films was measured by high-Q torsional oscillators [9]. High-T_c copper oxide superconductors were evaluated using similar torque magnetometry [10]. In another application of torque magnometry, the spread of the quantum ground state was evaluated in an array of aluminum (non-superconducting) rings on cantilevers with an external magnetic field, causing a noticeable shift in the cantilevers' resonance [11]. Lastly, the measuring torque on a doubly refracting plate assisted in detecting the angular momentum of light [12].

While torsional devices are sensitive, they are ineffective without a way to measure their motion. One of the current methods used to accomplish this is laser interferometry on one of the torsion paddles, where the optical contrast arises from the mechanical motion and the substrate [13]. While it is a viable method, it is limited by single photon sampling, yielding a low optical finesse. Electro-capacitive measurements through metal deposition on the torsion paddles [3] is another possibility, but noise-reduction demands nontrivial electrical circuitry. Another method for high mechanical sensitivity detection is optomechanics, which scales down well and is a good solution to this problem [14–16]. Cavity optomechanics has recently shown a high level of sensitivity for nanoelectromechanical system (NEMS) devices and has been used to accurately sense the mechanical movement of torsional resonators [17, 18].

1.2 An Introduction to Cavity Optomechanics

Cavity optomechanics describes the interaction between photons in an optical resonator and phonons in a mechanical device. The simplest concept of an optomechanical system to consider is a Fabry-Perot cavity with a movable mirror, an example of which is seen in Fig. 1.1. The Fabry-Perot cavity seen here, is composed of two parallel mirrors, with each of their reflective surfaces pointing toward the opposing mirror. One of the mirrors is stationary and not perfectly reflective, letting incident light on its backside into the optical cavity. The other mirror's motion is restricted by a spring, in the direction of the incident light. By shining a laser through the back of the stationary mirror, optical modes can be excited as the light is trapped between the two mirrors. An arbitrary optical mode can undergo small changes in its

resonant frequency due to the displacement of the movable mirror. The resonances of the mechanical system can best be sensed by tuning the laser to the side of an optical resonance. Usually an optical resonance possessing a high quality factor (Q ¿ 1) is chosen, which yields a greater change in the laser transmission for a given mechanical oscillation.

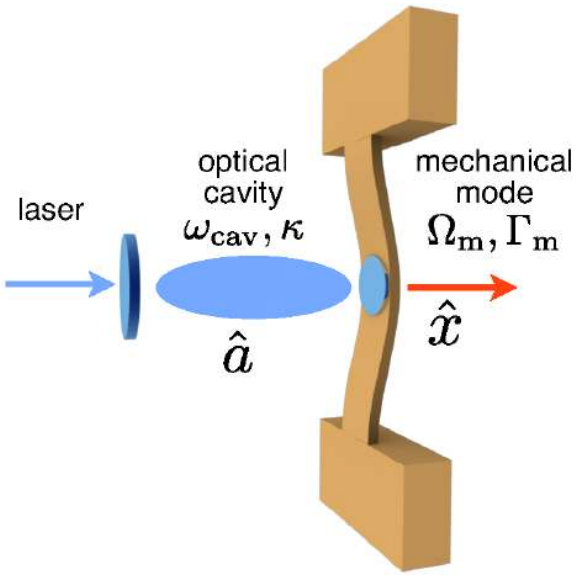

Figure 1.1: Sample Fabry-Perot cavity having stationary and movable mirrors with resonances ω_{cav} and Ω_m, damping factors κ and Γ_m, and amplitude vectors $\hat{a}$ and $\hat{x}$, optical and mechanical respectively [19]. In this thesis, ω_{cav} and Ω_m were on the order of THz and MHz with κ and Γ_m on the order of GHz and Hz, respectively.

Recently, gravitational wave detectors such as the Virtual Roentgen and Gamma Observatory (VIRGO) and the Laser Interferometer Gravitational Wave Observatory (LIGO), have employed Fabry-Perot cavities and Michelson interferometers. These detectors have only recently reached sensitivities down to the zeptometer scale, on the same order as as gravitational waves [20]. These detectors are limited by shot noise at low laser power and by radiation pressure force noise at high laser power. Shot noise originates from the discrete number of photons incident on, and the number of

charge carriers in, the detector. Conversely, the radiation pressure force noise results from the impacting flux of photons on the mirrors. These boundaries are related to the standard quantum limit (SQL). This limit originates in quantum optics from the two quadratures composing the in-phase (real) and out-of-phase (imaginary) amplitudes of the electric field measured simultaneously with equal precision [21,22]. Lately, LIGO and other mechanical detectors have been attempting to improve their sensitivity by generating squeezed states of light, using a nonlinear, potassium titanyl phosphate (PPKTP) crystal [23]. These squeezed states are able to measure one of the quadratures with great accuracy while increasing the uncertainty in the other.

Scaling-down techniques in recent decades have led to fabrication of on-chip optomechanical devices having masses on the order of picograms and whispering gallery mode (WGM) resonators on the order of microns [17, 24, 25]. WGM were first witnessed in St. Paul's cathedral where whispering acoustical modes appeared around the circumference of the circular cathedral when a sound source was placed next to and directed tangential to the wall [26]. These WGM were attenuated less than that of the sound propagating spherically from the source. Optical WGM can be contained in microdisks, bottles, toroids, and other circular fabricated devices using materials transparent in the spectrum being investigated. These optical WGM resonators have long photon lifetimes and are used to couple to nearby mechanical devices and breathing modes. The long photon lifetime of the WGM leads to the photons being able to interact with the nearby mechanics for a long amount of time, yielding enhanced mechanical sensitivity compared to that of the single-photon sampling in laser interferometry. The resulting WGM optical phase and resonant frequency are shifted by the adjacent mechanical motion. The radiation pressure of the WGM also has the ability to drive or dampen a coupled mechanical

resonator, depending on whether the laser is blue or red detuned from the cavity resonant frequency [21]. These properties are not exclusive to WGM resonators, but extend to other geometries as well, such as photonic crystal cavities [27], Fabry-Perot etalons [28, 29], and electronic microwave cavities [30].

The size of the WGM resonator and mechanics are bound by a couple of different factors, the first being the optomechanical coupling coefficient, G (Hz/m). The coupling is described as

$$\omega(z_0 + z) \approx \omega(z_0) + Gz, \tag{1.3}$$

where G is defined as

$$G = \frac{\partial \omega(z_0)}{\partial z}. \tag{1.4}$$

Here $\omega(z_0)$ is the unperturbed optical resonant frequency, $\omega(z_0 + z)$ the shifted optical resonance due to the mechanical movement, and z is the mechanical displacement. Hence, G is the shift in optical resonance per mechanical displacement. For WGM radial breathing modes, G is written as $\omega(z_0)/R$, as opposed to $\omega(z_0)/L$ for Fabry-Perot cavities, where R is the radius of the WGM cavity and L is the mirror separation distance of the Fabry-Perot cavity. For WGM resonators of more complex geometries, G cannot be determined as elegantly but requires simulations [31]. It is necessary to increase G as much as possible to increase the mechanical sensitivity.

The devices examined in this thesis are composed of a 38 μm diameter disk adjacent to a torsional resonator, which varied in the flange width (that is, the edge width of the mechanical device directly adjacent to the microdisk). Both of the resonators are comprised of 220 nm thick crystalline silicon, supported by 2 μm etched silicon dioxide. The disk acts as a WGM trapping photons around its edge, while the thermal fluctuations of the torsional resonator perturb the optical resonance

in the same way a spring-loaded movable mirror perturbs a Fabry-Perot cavity. A scanning electron microscope (SEM) image of one of the devices studied is seen in Fig. 1.2. In previous experiments, a single-mode, tapered, dimpled, optical fiber attached to a forked fiber holder was lowered and coupled to similar microdisks [18]. In this study, a single-mode, tapered, optical fiber was attached to an arched fiber holder, and then lowered onto the disk.

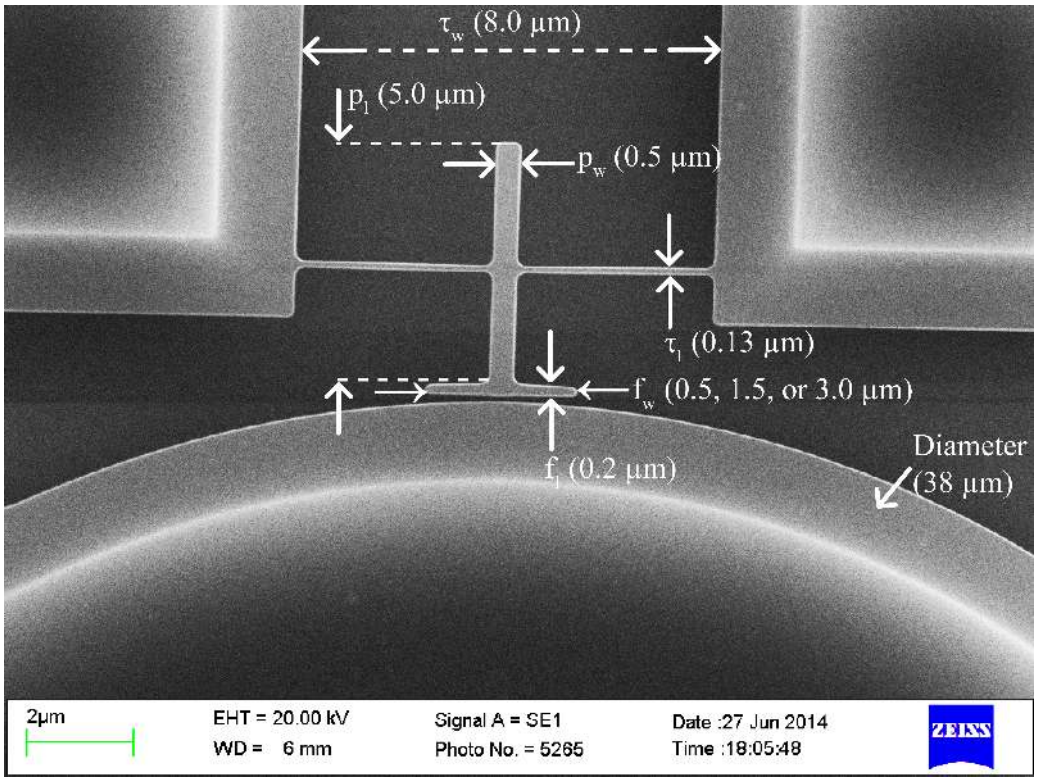

Figure 1.2: SEM image of one of the devices studied having a flange width of 3 μm. The torsional resonator is labeled as τ_{l} being the torsion rod length, τ_{w} the torsion rod width, p_{l} the paddle length, p_{w} the paddle width, f_{l} the flange length, and f_{w} the flange width. 130 nm beneath the torsional resonator is a microdisk which acts as a whispering gallery mode. The flange width varied between the three torsional resonators studied while all other dimensions were kept constant.

1.3 Calibrating Optical Modes

In order to sense the mechanical movement of the torsional resonator being studied, an optical resonance possessing a high quality factor must first be found. This quality factor is defined as

$$Q_{\text{opt}} = \omega_{\text{cav}}\tau = \omega_{\text{cav}}\kappa^{-1}, \tag{1.5}$$

where ω_{cav} is the resonant optical frequency of the cavity, τ is the photon lifetime, and κ is the cavity decay rate defined as the inverse of the photon lifetime. κ is comprised of two components, κ_{ex} being the loss rate due to coupling and κ_0 being the loss rate from other lossy sources. Conventionally, a mode having a quality factor greater than one is a high Q mode. The decay rate can then be described as

$$\kappa = \kappa_{\text{ex}} + \kappa_0. \tag{1.6}$$

In order to describe the photons inside the cavity, input-output theory must be consulted [32], which allows determination of the electric field amplitude, $\hat{a}$, inside the cavity. $\hat{a}$ has a decay rate of $\kappa/2$ and has an equation of motion of [21]

$$\dot{\hat{a}} = -\kappa\hat{a}/2 + i\Delta\hat{a} + \sqrt{\kappa_{\text{ex}}}\hat{a}_{\text{in}} + \sqrt{\kappa_0}\hat{f}_{\text{in}}, \tag{1.7}$$

where $\hat{a}_{\text{in}}$ is the input field from the laser and $\hat{f}_{\text{in}}$ is the quantum noise in the system. The laser is detuned off of the cavity's resonance by

$$\Delta = \omega_L - \omega_{\text{cav}}. \tag{1.8}$$

Here ω_L is the laser frequency. The frame of motion chosen for this formulation rotates at the same rate as the laser frequency

$$\hat{a}^{orig} = e^{-i\omega_L t}\hat{a}^{here} \tag{1.9}$$

and is normalized to the input power as

$$P_{\text{in}} = \hbar\omega_{\text{cav}}\langle\hat{a}^{\dagger}_{\text{in}}\hat{a}_{\text{in}}\ \rangle \tag{1.10}$$

where $\langle\hat{a}^{\dagger}_{\text{in}}\hat{a}_{\text{in}}\rangle$ is the average rate of photons coming into the cavity, $\hat{a}^{orig}$ is the original stationary frame of motion, and $\hat{a}^{here}$ is the rotating frame of motion. The light coupled back into the fiber waveguide is [19]

$$\hat{a}_{\text{out}} = \hat{a}_{\text{in}} - \sqrt{\kappa}\hat{a}. \tag{1.11}$$

To consider the classical case, the average must be taken of the field amplitude, which can be thought of as the time dependent amplitude of the electric field inside the cavity. For the classical case, the quantum noise in the system is eliminated ($\langle\hat{f}_{\text{in}}\rangle = 0$). Considering the separate steady state case gives an electric flux of zero ($\dot{\hat{a}} = 0$). This gives the overall average electric field amplitude as [33]

$$\langle\hat{a}\rangle = \frac{\sqrt{\kappa_{\text{ex}}}\langle\hat{a}_{\text{in}}\rangle}{\kappa/2 - i\Delta}. \tag{1.12}$$

The next step is to formulate an equation of the optical transmission after the light has coupled into the WGM, which will be used in the end to fit optical resonances and extract various properties (Q_{opt}, κ). The ratio of the average output to input

field is the transmission amplitude t,

$$t = \frac{\langle \hat{a}_{\text{out}} \rangle}{\langle \hat{a}_{\text{in}} \rangle}, \tag{1.13}$$

the square of which is the power of transmission through the fiber, T,

$$T = |t|^2, \tag{1.14}$$

which the same as the signal from the photoreceiver. Substituting Eq. 1.12 into Eq. 1.11 obtains

$$\langle \hat{a}_{\text{out}} \rangle = \langle \hat{a}_{\text{in}} \rangle - \frac{\kappa_{\text{ex}} \langle \hat{a}_{\text{in}} \rangle}{\kappa/2 - i\Delta}, \tag{1.15}$$

which can be used to solve for the transmission amplitude

$$t = \frac{(\kappa_0 - \kappa_{\text{ex}})/2 - i\Delta}{(\kappa_0 + \kappa_{\text{ex}})/2 - i\Delta}. \tag{1.16}$$

The fiber transmission is now

$$T = \frac{\kappa_0^2/4 - \kappa_{\text{ex}}\kappa_0 + \kappa_{\text{ex}}^2/4 + \Delta^2}{\kappa^2/4 + \Delta^2}, \tag{1.17}$$

which can be simplified using Eq. 1.6 yielding

$$T = 1 - \frac{\kappa_{\text{ex}}\kappa_0}{\kappa^2/4 + \Delta^2}. \tag{1.18}$$

However, when the fiber is touching the resonator, optical scattering reduces the transmission. From these scattering losses, an amplitude reduction factor of $T_0 < 1$

is necessary, giving

$$T = T_0 \left(1 - \frac{\kappa_{\text{ex}}\kappa_0}{\kappa^2/4 + \Delta^2}\right). \tag{1.19}$$

This equation can then be fitted to the optical resonance where κ and from that, Q_{opt}, can be extracted. While κ can be found from Eq. 1.19, it is not possible to differentiate between κ_0 and κ_{ex}, unless the same optical resonance is compared with the tapered fiber hovering at varying distances above the microdisk.

1.4 Calibrating Mechanical Modes

A mechanical mode can be studied after finding a high-Q optical resonance with the laser tuned to the side of the optical resonance. In order to extract the mechanical properties of the device from a given mechanical mode, a model must be made from the basic mechanics, from which, various mechanical properties can be extracted. The following proof is from [34]. The devices being investigated are torsional and can be modeled as a simple harmonic oscillator. For a particular mechanical mode, the governing equation for the time dependent displacement out of plane of the sample, $x(t)$, is a simple differential equation,

$$\ddot{x}(t) + \frac{\Omega_n}{Q_{\text{mech},n}}\dot{x}_n(t) + \Omega_n^2 x_n(t) = \frac{F(t)}{m_{\text{eff},n}} \tag{1.20}$$

where Ω_n is the resonant angular frequency of the nth mode, an effective mass for the nth mode $m_{\text{eff},n}$, a mechanical quality factor of $Q_{\text{mech},n}$, and a driving force $F(t)$. In this setup, the resonator was not actuated remotely meaning the driving force is purely thermomechanical. Each small volume element dV of a harmonic oscillator at $\vec{x}$ has a mass element of $dm = \rho(\vec{x})dV$, which corresponds to a potential energy

element of

$$dU = \frac{1}{2}\rho(\vec{x})\omega_n^2|a_n(t)\vec{r}_n(\vec{x})|^2 dV \tag{1.21}$$

where $a_n(t)$ is the function governing the time dependence of the resonator's motion, $\rho(\vec{x})$ is the position dependent density and $\vec{r}_n(\vec{x})$ is the displacement for the nth mode. From this, the total energy over the entire volume is

$$U = \frac{1}{2}\Omega_n^2|a_n(t)|^2 \int \rho(\vec{x})|\vec{r}_n(\vec{x})|^2 dV \tag{1.22}$$

$$U = \frac{1}{2}\Omega_n^2|a_n(t)|^2 m_{\text{eff},n} \tag{1.23}$$

with $m_{\text{eff},n}$ defined as

$$m_{\text{eff},n} = \int \rho(\vec{x})|\vec{r}_n(\vec{x})|^2 dV. \tag{1.24}$$

The normalized mode shape $\vec{r}_n(\vec{x})$ chosen is at the point of maximum displacement, coinciding with the edge of the mechanical resonator next to the optical microdisk, seen in Fig. 1.2. For another choice of normalization at $\vec{x}_0$, the following equation can be consulted

$$m_{\text{eff},n}(\vec{x}_0) = \frac{\int \rho(\vec{x})|\vec{r}_n(\vec{x})|^2 dV}{|\vec{r}_n(\vec{x}_0)|^2}. \tag{1.25}$$

The effective mass can be related to the effective moment of inertia by using the small angle approximation, $\theta \approx z/(l/2)$ where l is the total length of the torsion paddles. For all of the torsional resonators studied in this thesis, $l = 4.99 \pm 0.01\ \mu$m and is seen in the vertical direction in Fig. 3.5. The 0.01 μm error associated with l is inherent in the SEM. The effective moment of inertia can be related to the effective

mass as

$$I_{\text{eff},n} = \frac{l^2}{4} m_{\text{eff},n} \tag{1.26}$$

A similar differential equation to Eq. 1.20 can be made for torsion [34],

$$\ddot{\theta}(t) + \frac{\Omega_n}{Q_{\text{mech},n}} \dot{\theta}_n(t) + \Omega_n^2 \theta_n(t) = \frac{\tau(t)}{I_{\text{eff},n}}. \tag{1.27}$$

Taking the Fourier transform of Eq. 1.20 (1.27) and solving for $x_n(\Omega)$ ($\theta_n(\Omega)$) yields

$$x_n(\Omega) = \frac{F(\Omega)}{m_{\text{eff},n}(\Omega_n^2 - \Omega^2 - i\Omega\Omega_n/Q_{\text{mech},n})} \tag{1.28}$$

and

$$\theta_n(\Omega) = \frac{\tau(\Omega)}{I_{\text{eff},n}(\Omega_n^2 - \Omega^2 - i\Omega\Omega_n/Q_{\text{mech},n})}. \tag{1.29}$$

The displacement can be related to force by using a susceptibility term, $\chi(\Omega)$, as

$$x(\Omega) = \chi(\Omega) F(\Omega), \tag{1.30}$$

resulting in

$$\chi_z(\Omega) = (m_{\text{eff},n}(\Omega_n^2 - \Omega^2 - i\Omega\Omega_n/Q_{\text{mech},n}))^{-1} \tag{1.31}$$

and

$$\chi_\theta(\Omega) = (I_{\text{eff},n}(\Omega_n^2 - \Omega^2 - i\Omega\Omega_n/Q_{\text{mech},n}))^{-1}. \tag{1.32}$$

However, the experimental data collected from the spectrum analyzer is not displacement, but power spectral density, which is voltage squared normalized by bandwidth:

$$S_{vv}^{exp}(f) = \frac{V(f)^2}{BW} \tag{1.33}$$

where S_{vv}^{exp} is the experimental power spectral density in volts, $V(f)$ is voltage, and BW is the bandwidth. This power spectral density can then be fitted to extract the mechanical properties of the torsional resonator, as is shown below.

The power spectral density has two contributions, one on resonance $S_{zz}(f)$ ($S_{\theta\theta}(f)$), a noise floor S_{zz}^{nf} ($S_{\theta\theta}^{\mathrm{nf}}$), and a conversion term α (β) of units [$\mathrm{V}^2/\mathrm{m}^2$] ([$\mathrm{V}^2/\mathrm{rad}^2$]). The noise floor is the extracted sensitivity of the device.

$$S_{vv}^{exp}(f) = \alpha(S_{zz}^{\mathrm{nf}} + S_{zz}(f)) \tag{1.34}$$

$$S_{vv}^{exp}(f) = \beta(S_{\theta\theta}^{\mathrm{nf}} + S_{\theta\theta}(f)) \tag{1.35}$$

The power spectral density can also be gathered from the mean-square displacement, as seen in [34],

$$\langle z_n^2(\Omega)\rangle = \frac{1}{2\pi}\int_0^\infty S_{zz}(\Omega)d\Omega \tag{1.36}$$

which can be related as before with the susceptibility by the thermal force

$$S_{zz}(\Omega) = |\chi(\Omega)|^2 S_{FF}(\Omega). \tag{1.37}$$

This force $S_{FF}(\Omega)$ has only thermal contributions and is constant over the entire spectrum [34]

$$S_{FF}^{th} = 4k_B T m_{\mathrm{eff},n}\frac{\Omega_n}{Q_{\mathrm{mech},n}}. \tag{1.38}$$

Substituting this in to find the power spectral density function,

$$S_{zz}(\Omega) = \frac{4k_b T\Omega_n}{m_{\mathrm{eff},n}Q_{\mathrm{mech},n}((\Omega^2-\Omega_n^2)^2 + (\Omega\Omega_n/Q_n)^2)} \tag{1.39}$$

$$S_{\theta\theta}(\Omega) = \frac{4k_bT\Omega_n}{I_{\mathrm{eff},n}Q_{\mathrm{mech},n}((\Omega^2-\Omega_n^2)^2+(\Omega\Omega_n/Q_n)^2)} \tag{1.40}$$

or in terms of frequency,

$$S_{zz}(f) = \frac{k_bTf_n}{2\pi^3 m_{\mathrm{eff},n}Q_{\mathrm{mech},n}((f^2-f_n^2)^2+(ff_n/Q_{\mathrm{mech},n})^2)} \tag{1.41}$$

$$S_{\theta\theta}(\Omega) = \frac{k_bTf_n}{2\pi^3 I_{\mathrm{eff},n}Q_{\mathrm{mech},n}((f^2-f_n^2)^2+(ff_n/Q_{\mathrm{mech},n})^2)}. \tag{1.42}$$

This can then be substituted into Eq. 1.34 (1.35) to obtain the final equations

$$S_{vv}^{exp}(f) = \alpha\left(S_{zz}^{\mathrm{nf}} + \frac{k_bTf_n}{2\pi^3 m_{\mathrm{eff},n}Q_{\mathrm{mech},n}((f^2-f_n^2)^2+(ff_n/Q_{\mathrm{mech},n})^2)}\right) \tag{1.43}$$

$$S_{vv}^{exp}(f) = \beta\left(S_{\theta\theta}^{\mathrm{nf}} + \frac{k_bTf_n}{2\pi^3 I_{\mathrm{eff},n}Q_{\mathrm{mech},n}((f^2-f_n^2)^2+(ff_n/Q_{\mathrm{mech},n})^2)}\right). \tag{1.44}$$

A more thorough derivation can be found in [34].

After the mechanical data is collected, either of the above equations can be simplified into the below equation

$$S_{vv}^{exp}(f) = y_0 + \frac{Af_n}{Q_{\mathrm{mech},n}[(f^2-f_n^2)^2+(ff_n/Q_{\mathrm{mech},n})^2]} \tag{1.45}$$

where the fitting parameters are y_0, f_n, $Q_{\mathrm{mech},n}$, and A. After fitting, $Q_{\mathrm{mech},n}$ and f_n are easily extracted from the optimal fit parameters and the noise floor/sensitivity is obtained by

$$\text{noise floor}_z = \sqrt{\frac{y_0k_BT}{2\pi^3 Am_{\mathrm{eff},n}}} \tag{1.46}$$

$$\text{noise floor}_\theta = \sqrt{\frac{y_0k_BT}{2\pi^3 AI_{\mathrm{eff},n}}} \tag{1.47}$$

with $T = 300$ K for room temperature, $m_{\mathrm{eff},n}$ is calculated from the mode shape in

finite element modeling (FEM) simulations (as presented in Sec. 4.3), and $I_{\text{eff},n}$ is calculated from $m_{\text{eff},n}$ as seen in Eq. 1.26. It's worth noting that all equations for out of plane modes can be used for in plane modes as well.

Another property, which can be found from using both a mechanical resonance and the particular side of the optical resonance at which the mechanical data was obtained, is the optomechanical coupling coefficient, G. Eq. 1.4 can be expanded as

$$G = \frac{\partial\omega(z_0)}{\partial z} = \frac{\partial\omega(z_0)}{\partial V}\frac{\partial V}{\partial z} \tag{1.48}$$

with $\frac{\partial V}{\partial z}$ being $\sqrt{\alpha}$, α being the conversion factor first seen in Eq 1.34 [25]. $\frac{\partial\omega(z_0)}{\partial V}$ can be found by finding the inverse slope of the side of the optical resonance, in the frequency spectrum, at which the mechanical resonance data was gathered. For this particular setup, a New Focus 1811 photoreceiver was used which amplifies its AC output 4x more than its DC output. The end equation is then

$$G = \frac{\frac{\partial V}{\partial z}}{4\frac{\partial V}{\partial\omega(z_0)}}. \tag{1.49}$$

The optomechanical coupling coefficient can be combined with the zero point fluctuation amplitude, x_{zpf}, to obtain the single photon/phonon coupling rate, g_0, where [21]

$$g_0 = G x_{\text{zpf}} \tag{1.50}$$

and

$$x_{\text{zpf}} = \sqrt{\frac{\hbar}{2m_{\text{eff}}\Omega_{\text{m}}}}. \tag{1.51}$$

x_{zpf} can also be thought of as the spread of the position in the ground-state,

$$\langle 0|\hat{x}^2|0\rangle = x_{\mathrm{zpf}}^2. \tag{1.52}$$

Many thanks to Callum Doolin and Bradley Hauer for helping me with the derivations as well as programming the optical and mechanical fits.

1.5 Basis for Using a Photon STM

Cavity optomechanics applied to torsional devices has been seen in highly mechanically sensitive devices before [17], but an ultra-high vacuum (UHV, 10^{-11} mbar) environment is necessary for future applications such as electronic beam, molecular, and atomic deposition. The UHV chamber also offers high thermal stability from room temperature down to liquid helium temperature and is mechanically isolated from its environment. Samples can also be made in electronic beam deposition chambers and transfered into the P-STM chamber without breaking vacuum via an existing vacuum "suitcase". In the future, a torsional resonator could be mechanically actuated remotely through an alternating magnetic field by the deposition of magnetic thin-film permalloy and possibly manipulate magnetic states using alternating and constant magnetic fields.

The UHV chamber used in the study previously employed a Createc STM, and was chosen for the foundation for this study since it could be retrofitted with a tapered optical fiber using an arched fiber holder, as seen in Fig. 1.3. This tapered optical fiber would replace the STM tip and be used for coupling light into the microdisk. A computer generated image of a tapered fiber next to a microdisk and torsional resonator is seen in Fig. 1.4. After mounting a tapered fiber, some of the

innate STM features could still be used, such as scanning the surface optically instead of electrically. The device was dubbed a photon STM (P-STM) since an STM was used as the basis of this study and photons were being used to couple into the sample.

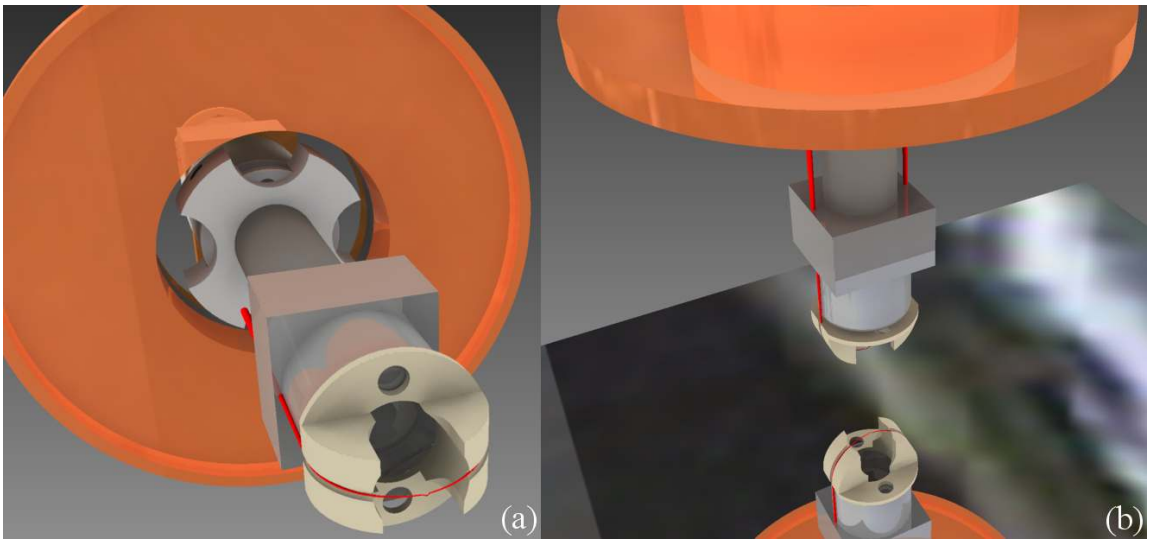

Figure 1.3: Preliminary computerized model of the P-STM viewed from the (a) bottom and (b) top.

One of the applications of the P-STM was to use its scanning technique to obtain an optical topography of the sample, instead of the typical electrical topography generated by an STM. In order to obtain the optical topography of a sample using a scanning technique, it is pertinent to first consult the conventional technique for scanning with an STM. A conventional STM has a vertical piezo attached to a sharp tip (conventionally tungsten) close to the sample (5-6 Å) with a bias voltage applied between the tip and the sample. The equation governing the tunnel current, J_{T}, between the tip and the sample is [35]

$$J_{\mathrm{T}} \propto (V_{\mathrm{T}}/s)exp(-A\phi^{1/2}s) \tag{1.53}$$

with ϕ being the mean value of the two electrode work functions, V_{T} the applied volt-

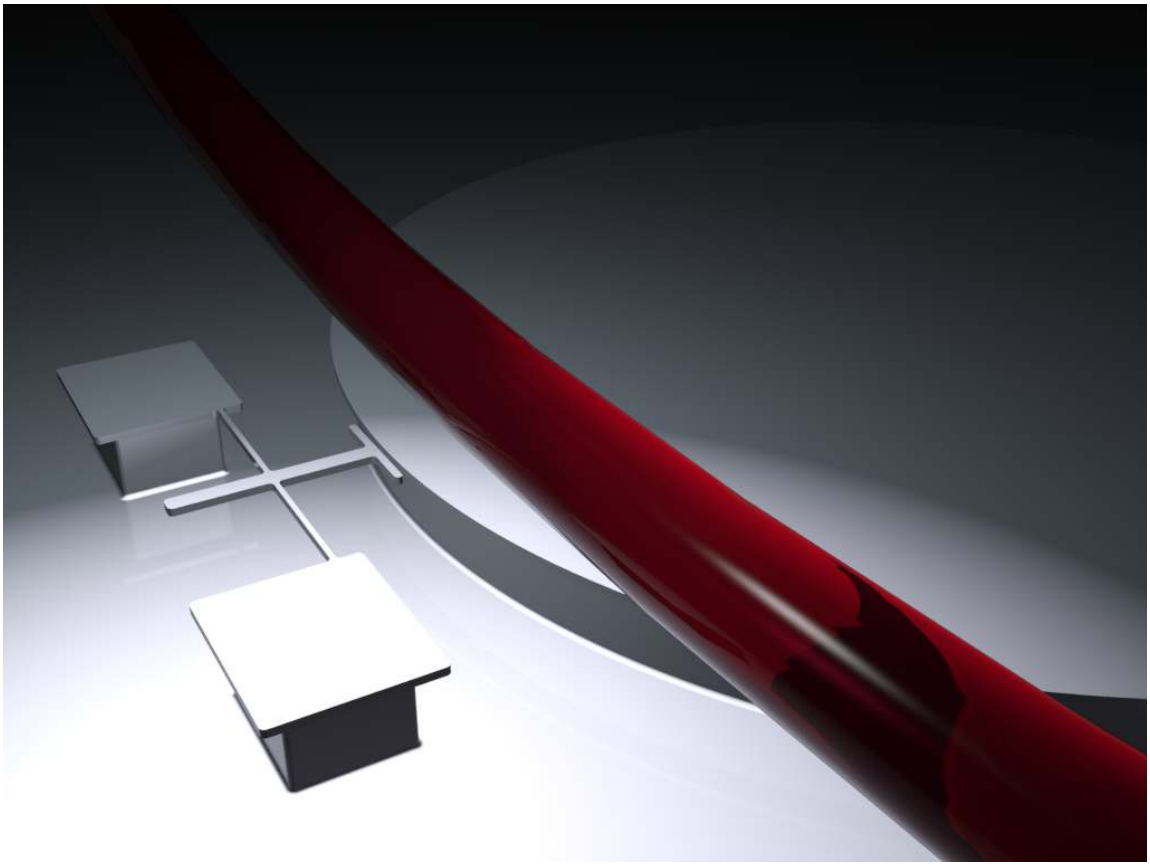

Figure 1.4: A computer generated image of a tapered fiber next to a microdisk and torsional resonator.

age between the electrodes, s the gap between the electrodes, and $A \approx 1.025(eV)^{-1/2}\text{Å}^{-1}$. A particularly valued aspect of this equation is that for work functions of just a few eV, a change of an angstrom of s yields a change of an order of magnitude in J_{T}. A diagram of an example STM can be seen in Fig. 1.5. The piezodrive is controlled by the control unit (CU) which sends voltages P_y and P_z to the piezo, thereby scanning in the y-direction while maintaining a constant tunnel current through slight changes in the z-direction. Using this method, an image representing the topography of the

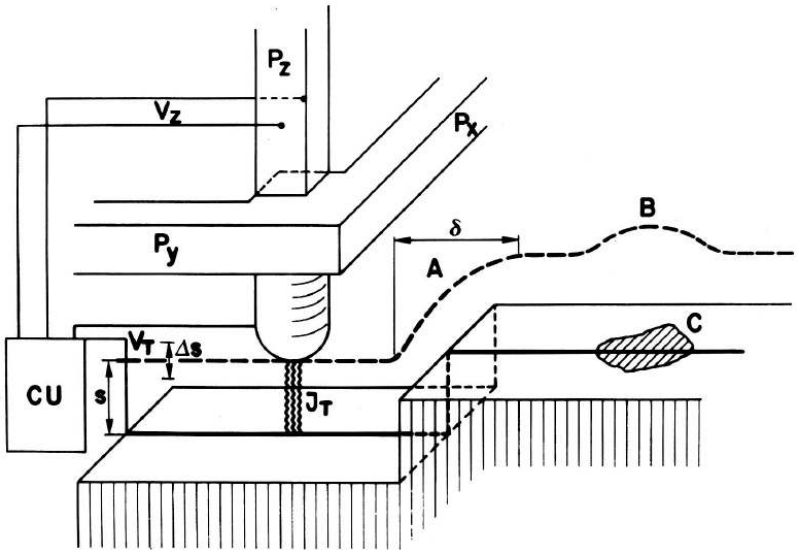

Figure 1.5: Diagram of a conventional STM [35].

sample can be generated, given a constant work function, $V_z(V_x, V_y)$. Thus for a step in the sample at A in Fig. 1.5, a constant distance, s, is maintained between the sample and the tip over the y distance of δ. While s is not usually known, the changes in the work function for keeping a constant tunnel current are accompanied by changes in s. This means that if the sample has an area of lower work function at C, the tip is moved away from the sample at B. Maintaining ϕ separately, the signal, J_s, is gathered during scanning by changing the gap between the sample and the tip

by Δs, illustrated in Fig. 1.5 and by the equation

$$J_s = \Delta(\ln J_\mathrm{T})/\Delta s \propto \phi^{1/2}. \tag{1.54}$$

While the P-STM used in this thesis does not have a "tunneling" aspect in the conventional sense, the same idea can be applied optically using an arched tapered fiber in place of the aforementioned tip and the tunnel current replaced by the optical transmission.

The sample used was 220 nm of single crystal silicon on a sacrificial layer of 2 μm thick silicon oxide. After etching, the etched device layer is left with a 2 μm gap between it and the silicon substrate. When the fiber is close enough to couple, the effective index of refraction of silicon (n $\approx$ 3.47) compared to that of air/vacuum (n $\approx$ 1.00) would cause a change in the optical transmission of the fiber. This method can be used to generate an optical topography image of the sample and would greatly facilitate aligning the fiber to optical resonators. Such optical topography images were not accurately obtained as of yet, due to time constraints, the taper scanning within one wavelength of the device layer for sensing, and other difficulties as documented in Section 3.5. With more time in the future, the obstacles could be overcome.

This thesis first discusses how a single-mode tapered fiber was made and mounted onto a custom fiber holder in Ch. 2. Ch. 3 explains how P-STM was built, after which the tapered fiber on a fiber holder was attached and used to couple to the device, yielding the optical and mechanical resonances. These resonances were later analyzed and the mechanical properties extracted in Ch. 4. While higher vacuums, optical topography by scanning the fiber, and coupling 10 μm disks were not possible due

to time constraints, the setup was proven to successfully couple to 38 μm diameter disks.

Chapter 2

Fiber Pulling

2.1 Theory of Fiber Pulling

Many optical resonator setups, especially those dealing with optical coupling to mechanical structures, require a waveguide or tapered fiber [36]. Its purpose is to couple the light (1520 - 1570 nm) to a nanoscale optical resonator. In order to mount a fiber in the P-STM, an arched holder was designed to hold the tapered fiber, in place of the conventional STM tip, and had a diameter close to 18 mm, per the constraints of the P-STM. Additionally, changes to the existing fiber pulling protocol were required.

To provide the needed evanescent field for coupling, the diameter of the taper must be less than 1.1 μm for a wavelength of 1550 nm [37]. This is accomplished by simultaneously heating and stretching the fiber lengthwise, which decreases its diameter exponentially with the pulling length [38]. The process is also known as "pulling" a fiber. The commonly used methods for doing this are by applying a CO_2 laser [39] [40] or a flame which travels along the section of the fiber being tapered [38]. A CO_2 laser heats proportional to the cross section of the fiber, therefore much

attention must be given to controlling the laser power with the changing length and diameter of the fiber [40]. A traveling flame heats relatively homogeneously independent of cross section and was therefore used. A taper of a relatively small length is needed in this setup, therefore a stationary flame was chosen, as opposed to a one which travels along the fiber during the pulling process.

2.2 Pulling and Mounting a Tapered Fiber

For heating, a hydrogen torch whose gas is controlled by a Whitey 22RS4 needle valve and a shut off valve is used. The torch is mounted on a three dimensional positioning system, composed of two computer controlled linear stages driven by stepper motors (Zaber T-LSM200A) for xy-positioning and a manual Mitutoyo micrometer for height adjustment. The 20 cm range and 50 nm step size of the linear stages are controlled either manually or by a computer. The Mitutoyo micrometer, having a range of 25 mm, is mounted to a right angle bracket which is then fixed to the two linear stages. This setup gives repeatability for x, y, and z positions as well as the ability to quickly move the torch away from the fiber after tapering. The fiber pulling and mounting setup are seen in Fig. 2.1 and is the same pulling setup described in [37].

A 125 μm SMF-28e fiber of roughly 2 meters long is stripped of its protective acrylic coating 2.5 cm from either end and 1 cm in the center. Both ends of the fiber are cleaved using an Ericsson EFC 11-4 fiber cleaver, coated with index match gel, and placed in mechanical fiber splicers. A New Focus Velocity 6330 diode laser produces 1550 nm light for monitoring the fiber transmission during pulling which is sent through the mechanical fiber splicer and the fiber to be pulled. The light is attenuated by a variable optical attenuator and detected by a New Focus 1811 IR

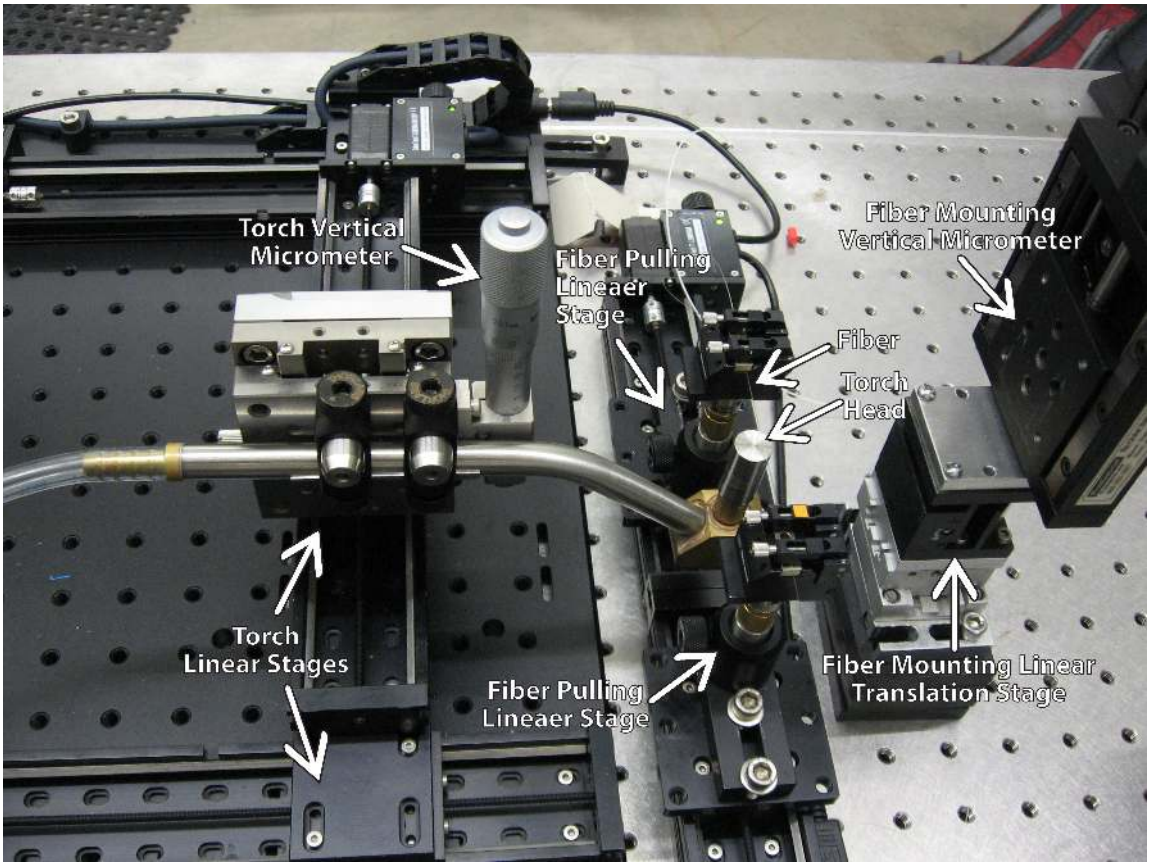

Figure 2.1: Fiber pulling setup with main parts identified.

DC-125 MHz Low Noise Photoreceiver. A NI USB-6259 BNC DAQ card receives the photoreceiver's signal for monitoring of the fiber's transmission.

The fiber is held in place using Newport fiber mounts, spaced 64 mm from each other and equidistant from the torch between them. The torch is positioned 3.0 mm downwards and 1.68 mm away in the horizontal direction from the center stripped section of the fiber, between the fiber mounts. The fiber mounts are each secured to the linear pulling stages by optical posts that can change the z-position of the fiber mounts, assisting in fiber alignment. The two linear stages driven by stepper motors (Zaber T-LSM100A), having 10 cm range and 50 nm single step size, are controlled manually and by a local computer. The custom torch head used has a 0.13 mm center inner diameter (ID), as opposed to 0.40 mm in the original version, both of which are seen in Fig. 2.2.

Figure 2.2: Custom torch head with 0.13 mm inner diameter hole (left) and previous torch head with 0.40 mm inner diameter (right)

Before pulling, the torch is moved a safe distance away from the fiber, lit, and placed in the aforementioned pulling position. The fiber is pulled at 40 μm/s via the Newport fiber-mounts on either side of the torch, while the transmission of the fiber is monitored. The transmission changes and oscillates during the pulling process

due to interference of modes in the fiber until only a fundamental mode exists. The transmission is constant, when the pulling process is stopped, and the torch pulled away from the fiber. If not, the fiber will break. An example of the fiber transmission is shown in Fig. 2.3. Losses of 45% and greater were observed, which is much greater than the 1% loss seen previously with this setup [37]. The greater losses are due to the shorter taper length, specifically from the transition region being less gradual between the original and tapered diameter of the fiber.

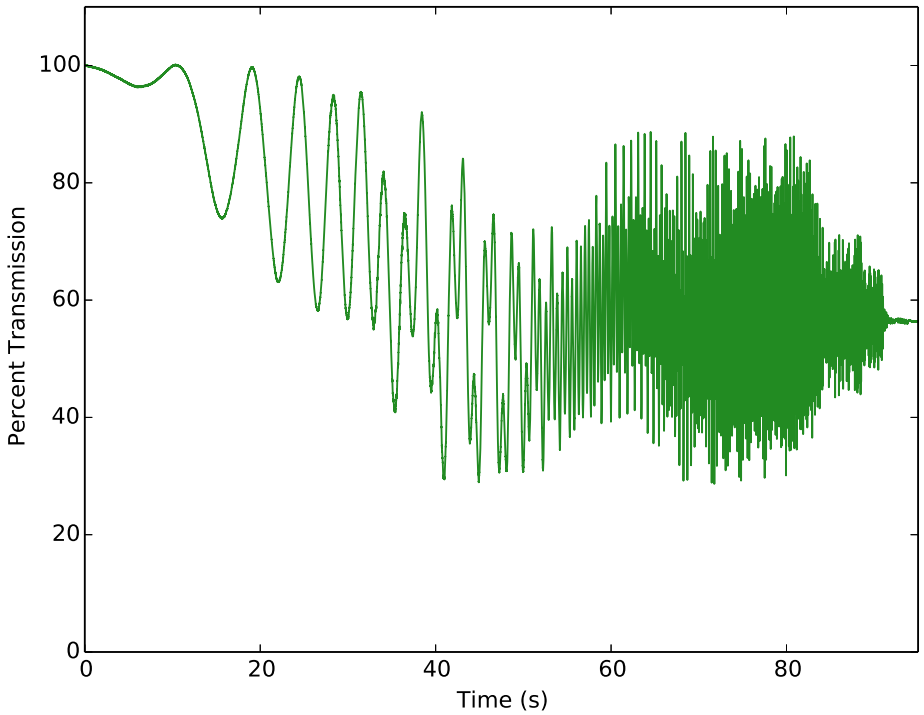

Figure 2.3: Sample transmission of fiber while pulling. Total pulling time was 95 seconds. End transmission: 55%. The oscillation in transmission is from interference of modes in the fiber, until the fiber is single mode at the very end.

After pulling a tapered fiber, it is glued to an arched fiber holder, two of which were designed and are shown in Fig. 2.4. The purpose of the fiber holder is to

support the taper and to secure it in the P-STM for optical coupling. They were designed to minimize weight, made with a groove running the curvature of the arch to guide the fiber during mounting, and to fit the constraints of the P-STM. The larger arched fiber holder was made to accommodate a longer taper while pushing the constraints of weight and size supported by the P-STM. In the end, the larger arched fiber holder was used. The arched holder is held and adjusted during the mounting process by a Newport DS40 xyz linear translation stage with a right angle bracket to fix a Proindustrial 124684 micrometer in the vertical direction. Another right angle bracket is employed to attach the fiber holder to the Proindustrial vertical micrometer. The fiber holder is secured to the bracket using a set screw. The translation stage has ranges of 14 mm (x and y), 5 mm (z) and a resolution of 1 μm, while the micrometer has a range of 25 mm and a resolution of 0.01 mm. The mounting setup and alignment of the arched holder is shown in Fig. 2.5.

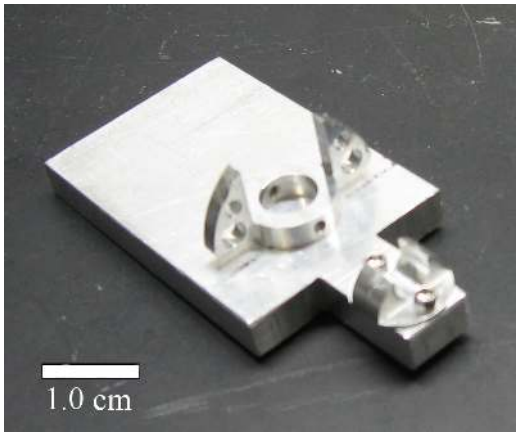

Figure 2.4: Custom, larger arched fiber holder (center) with a 10 mm center gap, compared to the previous, smaller fiber holder (lower-right) with a 5 mm gap. Both holders have a groove running the curvature of the arch to guide the fiber during the mounting process.

The arched holder is oriented such that its center coincides with that of the fiber and aligned with its groove along the length of the fiber. A microscope for monitoring

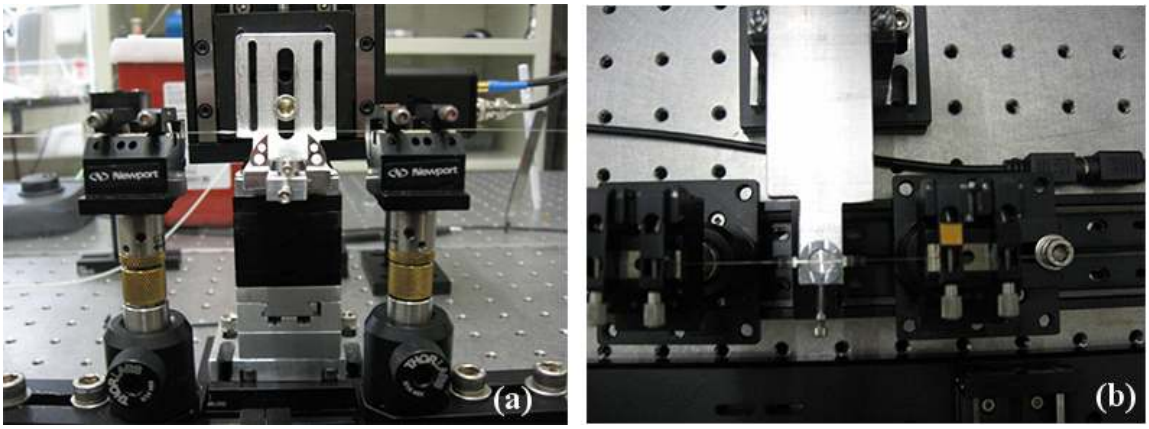

Figure 2.5: (a) Vertical and (b) horizontal alignment of the arched fiber holder.

the tension of the fiber and the position of the arched holder is attached in place of the torch. The microscope is composed of an Optem Zoom 70XL lens system on a 10X MPlan Apo long working distance objective, illuminated with an external Metaphase MP-LED-150 microscope LED, and digitally encoded with an Edmund Optics EO-5012C color USB webcam. The microscope with a tapered fiber glued to the arched fiber holder is seen in Fig. 2.6(a).

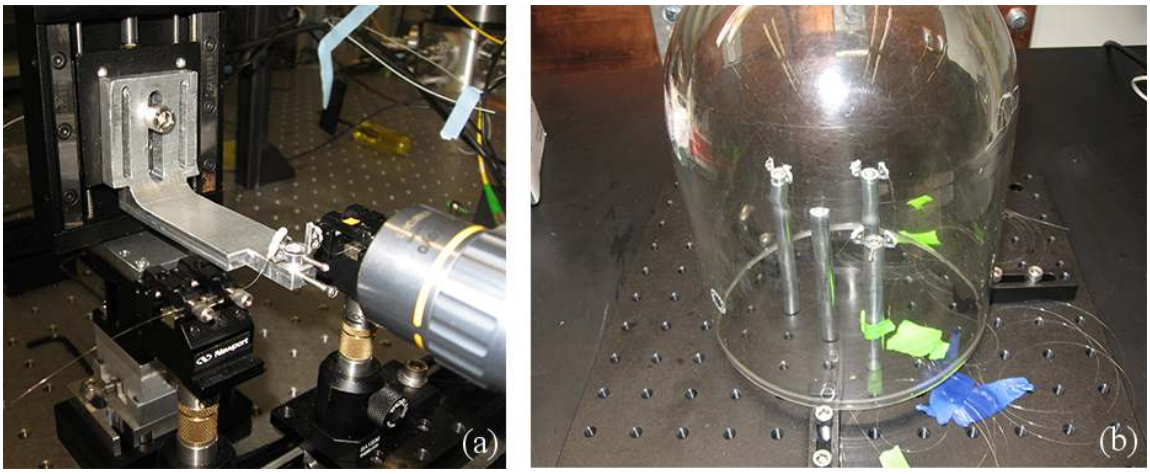

Figure 2.6: (a) A mounted and glued tapered fiber with microscope, after which it is placed in (b) a transport stage with a bell jar cover.

After the fiber holder is raised so that it barely contacts with the fiber on either

side of the taper, the fiber is detensioned intermittently while the holder is raised further. The raising action of the holder pushes the fiber upwards, bending the fiber around the holder with a sharp curve at the center. Detensioning is needed to not break the taper and increase the curvature of center taper. In the course of this step, the microscope is remounted to a higher position on its micrometer, due to the latter's range limitation. After the fiber holder is raised high enough so that the fiber lies tangentially to either of the highest points on the holder, as seen in Fig. 2.7(c) and (d), it is glued using Devcon 5 Minute Epoxy Gel. The epoxy was chosen for its short curing time and because it can be easily removed with acetone. Following the solidification of the glue, the fiber is further detensioned and holder raised until the fiber has fully wrapped around the holder and glued a final time for stress relief. Images of the fiber during the mounting process can be seen in Fig. 2.7. Next, the glued fiber is removed from the bare fiber splicers, coiled, and taped to a transferring stage, seen in Fig. 2.6(b), which the fiber holder is transferred to as well. The transferring stage is covered with a bell jar, which helps protect it from airborne contaminants.

2.2.1 Modifications to Pre-Existing Fiber Pulling Procedures

While the pulling procedure for fibers with tapers on the order of centimeters was performed with basically this system in the past, it needed many changes in not only the pulling procedure, but in the hardware as well, since this setup had never been used before to pull fibers with tapers less than a centimeter long or fasten them to a curved holder.

The first step which needed to be overcome was pulling a taper of length less than that of the center gap of the fiber holder. In order to accomplish this, a small hot-

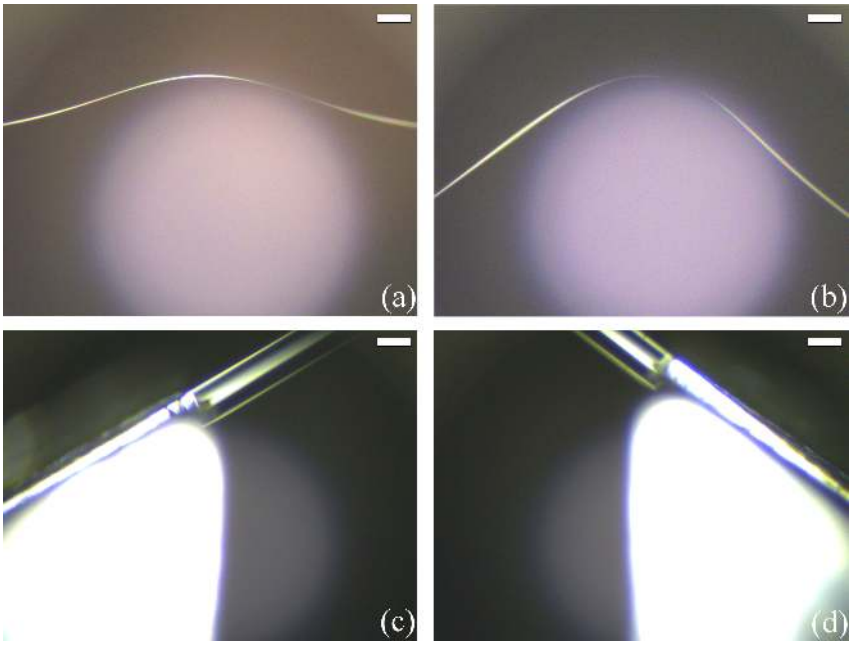

Figure 2.7: (a) Tapered fiber, slightly detensioned. (b) Center tapered fiber before gluing. (c) Left and (d) right side of fiber with fiber holder before gluing. Scale bars are 125 μm.

zone (heated length of the fiber while pulling) is required for shorter taper lengths. This aspect is further described by the equation [41]

$$r_{\mathrm{t}}(z_{\mathrm{t}}) = r_{\mathrm{t0}} e^{-z_{\mathrm{t}}/L_0}, \tag{2.1}$$

where r_{t0} is the initial radius of the fiber, $r_{\mathrm{t}}(z_{\mathrm{t}})$ is the end radius of the fiber, L_0 is the hot-zone length, and z_{t} is the taper length. Since $r_{\mathrm{t}}(z_{\mathrm{t}})$ is bound by the radius for a single mode (550 - 947 nm) and r_{t0} is 125 μm for the SMF-28e fiber used, z_{t} should be minimized, which means L_0 needs to be made as small as possible while still providing a relatively even taper. The 0.40 mm ID torch head's hot-zone length was too large for the short taper needed, even after reducing the flame size as much as possible.

Faster pulling speeds, from the typical 40 μm/s used previously, to 200 μm/s, were used in an attempt to shorten the taper length, but yielded relatively the same result as slower pulling speeds except with shorter pull times, as predicted by Eq. 2.1. Oxygen was used in conjunction with hydrogen in an attempt to decrease the hot-zone length with the 0.40 mm ID torch head, which did decrease the size of the flame substantially, and therefore the hot-zone length, but the amount of oxygen needed to hold the small flame size was extremely small and hard to control, even after installing a needle valve. The small flame size was also not consistent enough in its heating of the fiber to provide successful tapers.

Following these attempts, two changes were made concurrently. The fiber holder was redesigned in an endeavor to make its center gap larger, while limiting its weight so that it would not be too heavy for the attocube ANPz30 z-piezo in the P-STM setup. The attocube has a weight limitation of 10 g which needs to accommodate not only the fiber holder, but another piezo and the adjoining brackets. A new custom torch head was machined with a 0.13 mm outlet, smaller than the initial torch head used which had a 0.40 mm outlet. The combination of both of these was able to surmount the taper length dilemma with one drawback: the larger fiber holder was not as maneuverable on the P-STM.

The next obstacle which needed to be overcome was forming the fiber around the arched fiber holder. Since the Newport fiber-mounts would be used to hold the fiber *in situ*, a z-translational micrometer was employed to elevate the holder high enough so that the fiber could encompass the entire arch of the fiber holder.

A two-stage gluing technique was used, with the fiber running tangentially to the arch before gluing, to alleviate fiber strain. Strain on the fiber continued to heavily degrade its transmission during the forming process between the gluing stages. The

fiber was found to be more robust against this strain if it was not stripped of it acrylic coating on the sections being glued to the holder. Hereafter, the center region of the fiber stripped for tapering was constrained to be less than that of the arched gap of the fiber holder.

In the end, a successful technique was made for tapering and mounting a single-mode fiber which can be attached to the P-STM. Following, in 3, the P-STM was constructed, the tapered, mounted fiber attached, and optical and modes coupled to.

Thanks to other members of Davis group, especially Bradley Hauer, Callum Doolin, and Paul Kim for familiarizing me with pulling fibers and helping me come up with a new procedure including the two-step gluing process. David Fortin's help was greatly appreciated in designing the new fiber holder and torch tip as well as thinking of other possible ways to mount/pull a fiber for the P-STM setup.

Chapter 3

Experimental Setup

3.1 P-STM Setup

The P-STM is composed of a base, a movable independent head, and a removable sample holder contained in a UHV chamber. A New Focus TLB-6300-LN laser provides the necessary telecom wavelength light, which is sent into the chamber, through the tapered fiber (made in Ch. 2) coupled to the device, and back out of the chamber where it is detected. A telescope provides viewing for aligning the fiber with the optical resonator. The original Createc STM was altered in a variety of aspects to provide the necessary fiber coupling and greater robustness.

3.1.1 P-STM Base

The P-STM base is made of a sample holder stage and three coarse, stick-slip piezos, and a two-part frame. Both parts of the frame are oxygen free copper with gold over nickel coating. The two-part frame is held together with 316 stainless steel bolts. The bottom frame is bolted to three posts (originally springs) which are secured

similarly to the above inner cryostat.

The sample holder stage is pushed upward by a spring on the lower P-STM frame, clamping the sample between itself and the upper P-STM frame. Pulling down on the sample holder stage releases the sample holder. Both the sample holder and sample holder stage have copper contacts mounted on PEEK (polyether ether ketone) brackets for direct wiring to the sample, for future applications.

The base of the sample holder is of the same composition as the P-STM frame. An aluminum top elevates the sample from the sample holder base and is attached to the sample with double sided tape. For future UHV application, beryllium copper clips can be bolted to the aluminum top, to substitute for the double sided tape.

The coarse movement of the P-STM head containing the tapered fiber, is controlled by three stick-slip piezos, each glued with Epotek H77 to a sapphire sphere on its top and glued to the upper P-STM frame on its base. (Unless otherwise specified, Epotek was the glue used everywhere on the P-STM.) The wire for the inside contact on the stick-slip piezos was passed through protective PEEK tubing, between the top and lower P-STM frame, and then through a hole in the upper P-STM frame, at the base of each piezo. The outer contacts were wired at the base of each piezo. The stick-slip motion of the sapphire spheres moves the bottom copper walking surface of the P-STM head. Each part of the P-STM base is identified in Fig. 3.1.

3.1.2 P-STM Head Assembly

The P-STM head is comprised of an oxygen free copper disc with a retaining edge having four hollow aluminum posts bolted on at the top. These posts serve as vertical spacing, and are bolted to an oxygen free copper bracket. An attocube ANPz30 z-piezo, used for lowering and raising the fiber as much as 5 mm, is bolted to the top

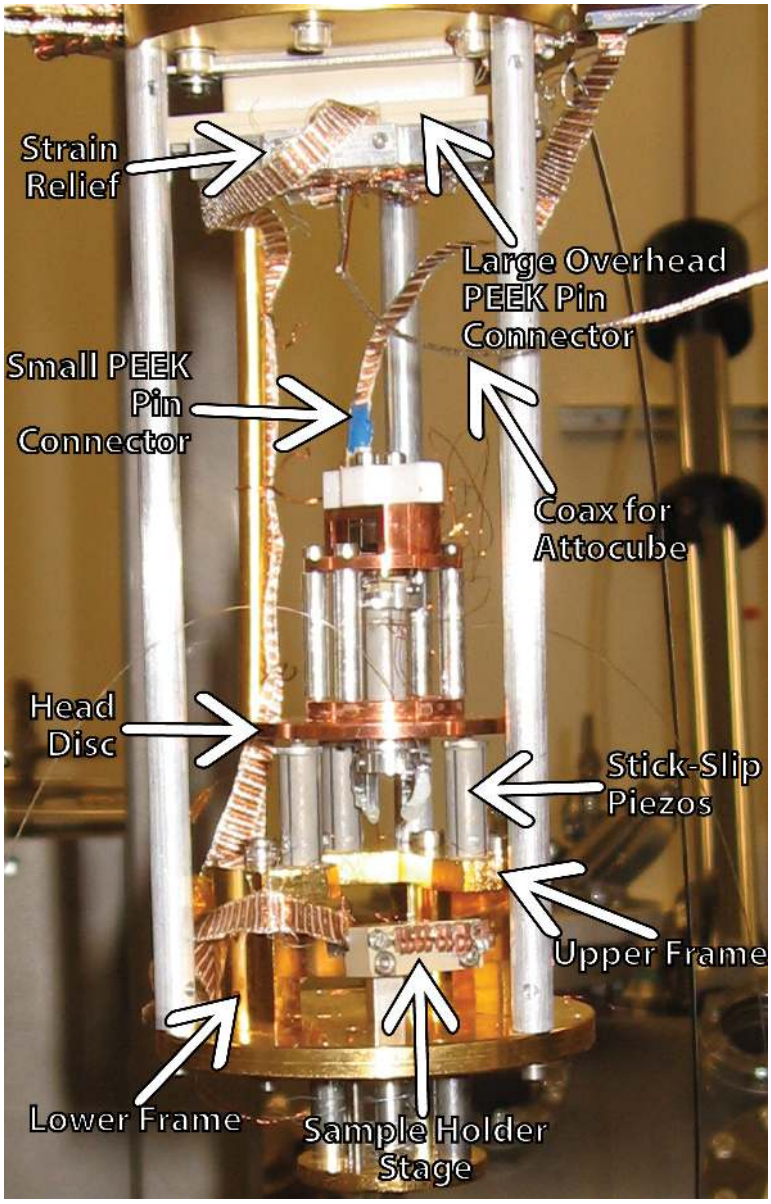

Figure 3.1: The P-STM with the upper frame, lower frame, sample holder stage, stick-slip piezos, head disc, small PEEK pin connector, large overhead PEEK pin connector, and strain relief for the large overhead PEEK pin connector identified.

copper bracket, the former of which is bolted to an intermediary aluminum bracket, glued to a PT-Tube Piezo scanner with a max xy deflection of $\pm$ 16 μm and max z deflection of $\pm$ 4.5 μm. The piezo is used for fine x and y movement with another aluminum bracket glued to its bottom which is secured to the fiber holder using a set screw. In wiring the head, a Macor (a machinable ceramic) connector bolted to the top copper bracket was machined to hold pins which connect the individual Kapton coated wires from the piezos and the wire loom via a small PEEK pin connector (Omnetics Part Number A79624-001). All wires were soldered with 157 solder and flux. The P-STM head can be seen in Fig. 3.2.

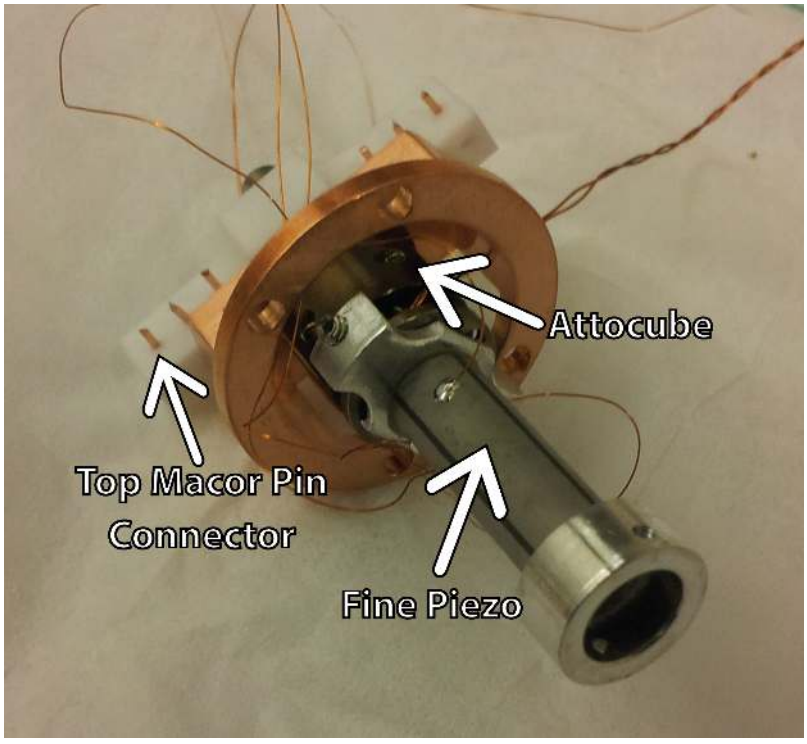

Figure 3.2: P-STM head with the fine piezo, attocube, and top Macor pin connector identified. The four aluminum posts and lower copper disc are not present.

3.1.3 Wiring the P-STM

Many difficulties were encountered when using the original wiring scheme of Kapton coated wires for the entire P-STM. The Kapton coated wires would at times short, from wires touching where the coating had worn away, or break, from the lack of strain reliefs, especially at the large overhead PEEK pin connector. This, coupled with the lack of organization of the wires seen in Fig. 3.3, led to rewiring the entire P-STM with Cryoloom wire loom. Each wire loom has 12 pairs of Kapton coated wires threaded in PEEK. Three looms ran from the overhead PEEK pin connector: one to the P-STM base, one to the PEEK bracket on the sample holder stage, and one to a small PEEK pin connector for the head. Another loom, mentioned previously, ran from another small PEEK pin connector to the Macor connector bolted to the top of the P-STM head. The process of changing tapers on the P-STM was greatly eased using this method, since the head could be completely removed by disconnecting the small PEEK pin connector. To strain relief the looms, narrow sheets of aluminum were bolted to the lower P-STM frame and the large overhead PEEK pin connector. Also, PEEK tubing was placed around the loom at the aluminum sheets. Additionally, the looms were glued with Tra-Bond 215 to the small PEEK pin connector for the P-STM head. The Tra-Bond presented an advantage over the commonly used Epotek in this instance since it does not require baking to cure and is still UHV compatible. The only remaining original Kapton coated wires ran from the center contact of the coarse piezos, on the upper P-STM frame, to the local wire loom and those previously mentioned running from the piezos on the P-STM head to the top Macor pin connector.

The resistance (200 ohms) of the wires running the length of the cryostat changed the time constant for the sawtooth wave sent to the attocube. The time constant

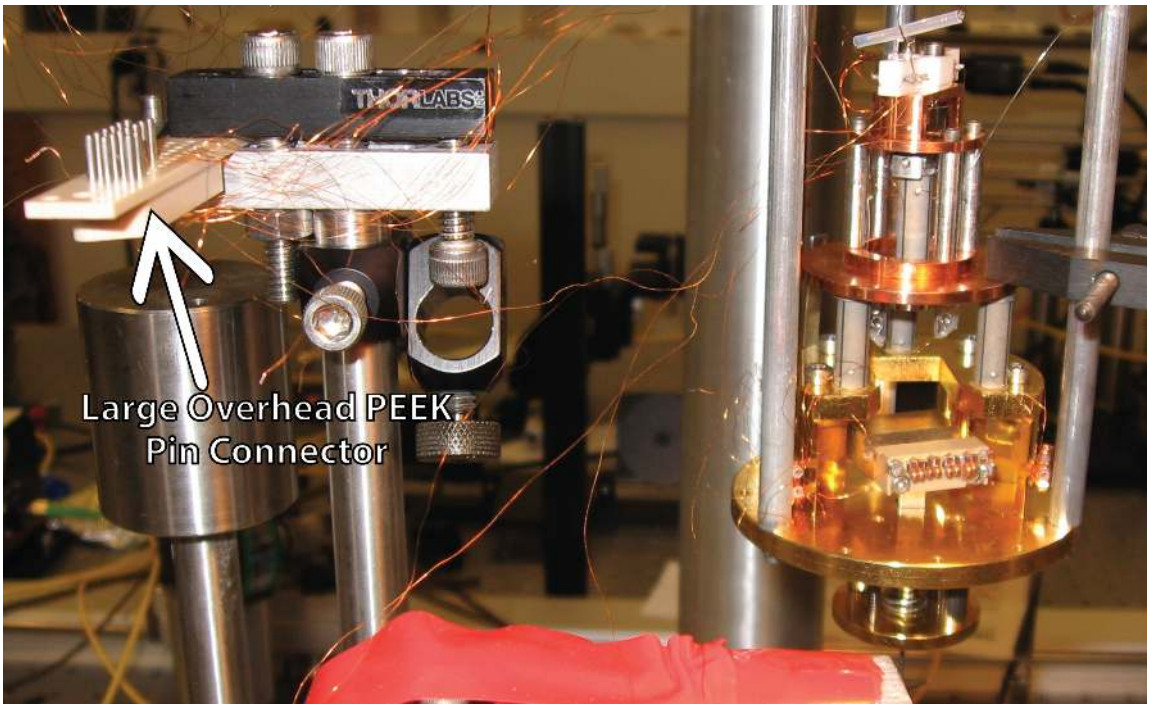

Figure 3.3: Wiring previously done with Kapton coated wires, which were later replaced with wireloom, seen in Fig. 3.1.

equation,

$$\tau = RC, \tag{3.1}$$

shows that for a given capacitance, changing the resistance of the circuit changes the time constant and hence the sawtooth wave. This led to using a separate Accu-Glass coaxial cable between the large overhead PEEK pin connector to a feedthrough at the base of the cryostat.

3.1.4 P-STM Chamber

3.1.5 Telescope

In order to view the alignment of the taper and the sample to accomplish optical coupling, a Questar QM100 telescope's image is sent to a computer using a Lumenera Lw235C 2.0 megapixel camera. The telescope's angular deflection and height is governed by a custom hinged platform and a Newport NRC 270 elevation stage. Also, the telescope's vertical and horizontal viewing angle can be controlled by another Questar 53600 platform. The telescope's position, relative to the P-STM in chamber, can be seen in Fig. 3.4.

3.1.6 Optical Circuit

The optical circuit of the system contains a New Focus TLB-6300-LN laser connected to a fiber polarization controller, which then sends the light to a variable optical attenuator. After this, the light passes through an optical fiber feedthrough into the chamber, through the taper, out of the chamber through another optical feedthrough, and detected using a New Focus 1811 photoreceiver. The DC component from the photo detector is sent to a National Instruments BNC-2110 DAQ card which is then

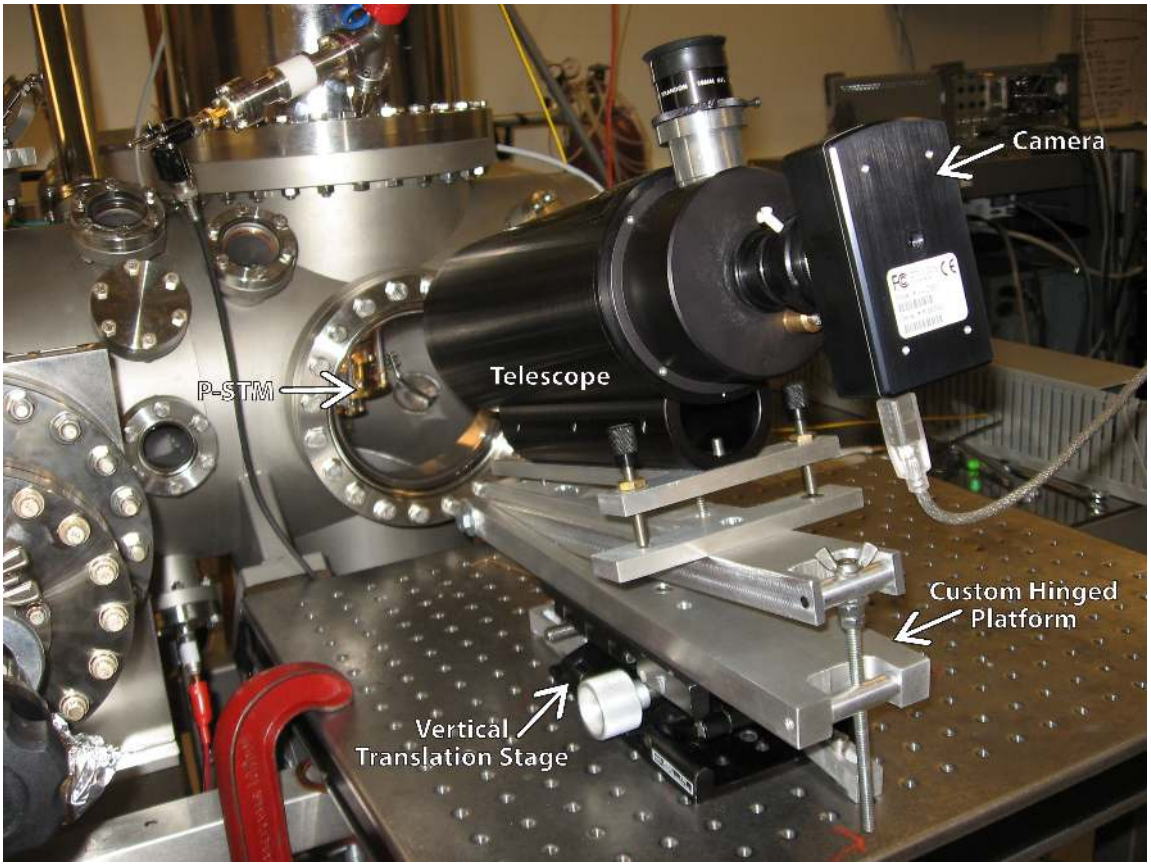

Figure 3.4: The overall setup containing the Questar telescope with a camera used for viewing the P-STM in chamber, through a glass port. The custom hinged platform, the vertical translational stage, and the telescope's platform are used for alignment of the telescope.

processed by LabView. The AC output from the photo detector is either sent to a Hewlett Packard 8594E spectrum analyzer or a Zurich HF2LI lock-in amplifier. Both the laser and the spectrum analyzer can be controlled locally or by LabView via a GPIB-USB-HS Controller.

3.1.7 Preparing the P-STM for coupling

A fiber is first tapered and mounted, as described in Ch. 2, after which it is transported to the P-STM lab for installation. The P-STM head is removed from the P-STM, the latter of which is hanging from the inner cryostat. The recently tapered fiber is installed on the bottom of the P-STM head with a set screw and the fiber directed through the center of the P-STM head disc. After this, the small PEEK pin connector on the head is reconnected and the head re-installed.

Dangling from the base of the cryostat shell are LewVac single mode vacuum compatible optical patch cables (FO-SM1300VC-1000), which have been previously fusion spliced to a bare 125 μm SMF-28e fiber using an Ericsson FSU 995 PM Fusion Splicer. The splices are protected with Kapton tape. The fiber from the taper is spliced similarly to the fiber already spliced to the optical patch cables. The SMF-28e optical fiber between each of the optical patch cables and the tapered fiber is used as a sacrificial intermediary, so that during future splicing, its length will shorten instead of that of the patch cable's. Finally, the fiber holder is oriented such that the plane of the arch is perpendicular to the line of sight of the telescope.

The sample holder is then inserted and the cryostat lowered into the chamber with a copper gasket between the cryostat and the chamber. After bolting down the cryostat, a BOC Edwards XDS 10 scroll pump is turned on and the vacuum measured with a ConvecTorr P-type thermo-couple pressure gauge. When the pressure is

3.0×10^{-3} mbar, a Varian TV301 Nav turbo pump is activated and the pressure monitored both at the load lock chamber and P-STM chamber with ion gauges, giving a vacuum down to 10^{-7} mbar.

3.2 Fabrication of Optical and Mechanical Resonators

The devices were fabricated from silicon-on-insulator with a 220 nm device layer of single-crystal silicon on top of a 2 μm sacrificial layer of silicon dioxide with a handle layer of amorphous silicon beneath. Patterning of the devices was done through CMC IMEC using 193 nm deep UV lithography. Subsequently, the wafer was diced and the chips released though a buffered oxide etch, removing 2 μm of silicon dioxide.

All of the optical microdisks studied had a diameter of 38 μm and the mechanical devices investigated had a torsion rod length (width) of 0.13 (8) μm and a paddle length (width) of 5.0 (0.5) μm. The difference in the three mechanical resonators inspected varied in flange width (section of the paddle adjacent to the microdisk) and changed from 0.5 μm (that of the width of the paddle) to 1.5 μm to 3.0 μm. The flange length was kept constant at 0.2 μm and the gap between the torsional resonator and the microdisk was 130 nm. SEM (scanning electron microscope) images of one of the devices, with the dimensions shown, and the three different devices used are seen in Fig. 1.2 and Fig. 3.5, respectively.

Thanks to Paul Kim for fabricating all of the chips and taking the SEM images for me.

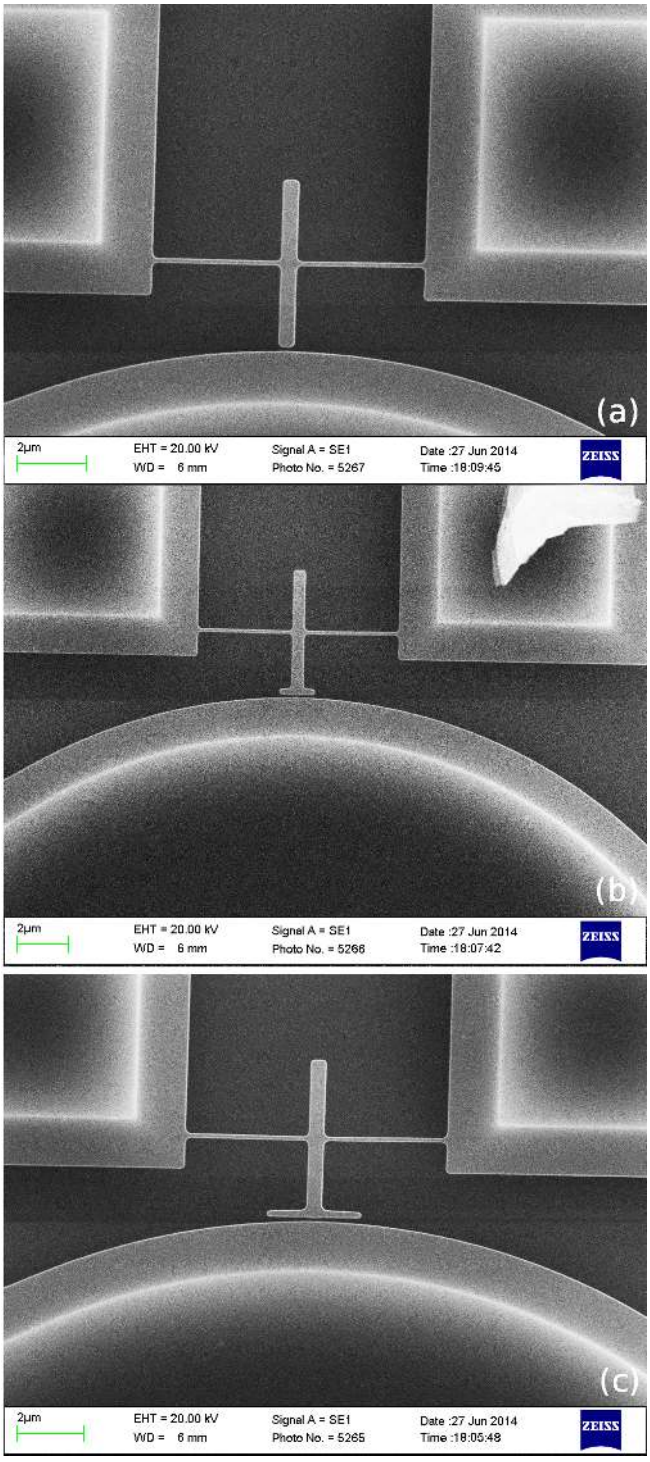

Figure 3.5: SEM images of all three mechanical resonators with flange widths of (a) 0.5 μm, (b) 1.5 μm, and (c) 3.0 μm. (The flange is the section of the mechanical resonator, nearest the optical microdisk.) Widths for all features are in the horizontal direction with lengths in the vertical direction. Credit goes to Paul Kim for taking these images.

3.3 Coupling to an Optical Resonator

When the P-STM is in a sufficiently high vacuum (10^{-7} mbar currently), the tapered fiber is moved to the xy position of the optical microdisk being investigated and rotated above the sample, using the coarse piezos and a Createc STM-AFM program. Images of the fiber in the typical orientation for coupling are seen in Fig. 3.6. A cropped version of the fiber outlined when above and when coupling to a 38 μm diameter disk in chamber is seen in Fig. 3.7. For coupling to a microdisk, the taper is placed along the edge of the disk, running tangentially. The taper is lowered through use of the attocube, by applying separately and in order: a continuous voltage, a stepped voltage, and an offset voltage. The continuous voltage provides a repeated sawtooth waveform signal to the attocube, lowering the fiber steadily. A stepped voltage sends one sawtooth signal to the attocube thereby lowering the taper incrementally. An offset voltage is a constant DC voltage sent to the attocube which directly changes the vertical position of the fiber by the smallest amount possible. While approaching the sample, the fiber's DC transmission is monitored though National Instruments Measurement and Automation Explorer program and stopped when the transmission decreases due to optical losses from the taper touching the sample. The transmission after touching may be anywhere from 0 to 70 % of that when not touching, due to optical scattering losses. If the transmission is too low during contact (usually anything less than 40 percent), the offset may be decreased or the fiber holder stepped up to reduce physical strain on the taper, reducing the optical scattering, thereby regaining some of the signal. To check for optical resonances, a LabView wavelength scanning program is run which scans the laser's full range (1519-1570nm) and monitors the DC optical signal. This scan is normalized with a background scan in which the fiber is not touching or in proximity to the sample.

An example of a normalized scan is seen in Fig. 3.8, the free spectral range is 6.1 - 6.5 nm (750 - 800 GHz).

3.4 Coupling to a Mechanical Resonator

To measure the resonance of the nearby mechanical structure after coupling to the local optical microdisk, the optical spectrum is examined for high Q modes ($Q > 1$). An example of such a mode is seen in Fig. 3.9. After selecting a high Q optical mode, the laser is tuned to one of the mode's high-sloped sides. Usually the red side of the optical resonance provided greater sensitivity to mechanical modes, due to optical heating. A spectrum analyzer was used for examining the AC optical signal in the possible mechanical resonance range (1 - 10 MHz), using a 100 Hz bandwidth. When searching for mechanical resonances in this range, the spectrum analyzer examined 200 kHz sections of the AC signal, scanning every 10 seconds. Each 200 kHz section was scanned at least twice (20 seconds in total at least), to ensure accurate readings, before examining the next section. A mechanical resonance is identified when a sharp upwards spike is seen in the signal amplitude, as seen in Fig. 3.10. The upward shape of the spike is from the amplitude of alternating component of the optical signal being the largest on the mechanical resonance frequency. Moving away from the center of the spike, the optical signal oscillates with less amplitude, since the tuning of the signal is slightly off of the mechanical resonance.

Further fine tuning of the laser on a high Q optical resonance serves to find the steepest slope of the optical resonance and increases the amplitude of the mechanical resonance. Following, the optical signal is attenuated or polarization changes using the variable optical attenuator or fiber polarization controller, respectively. The

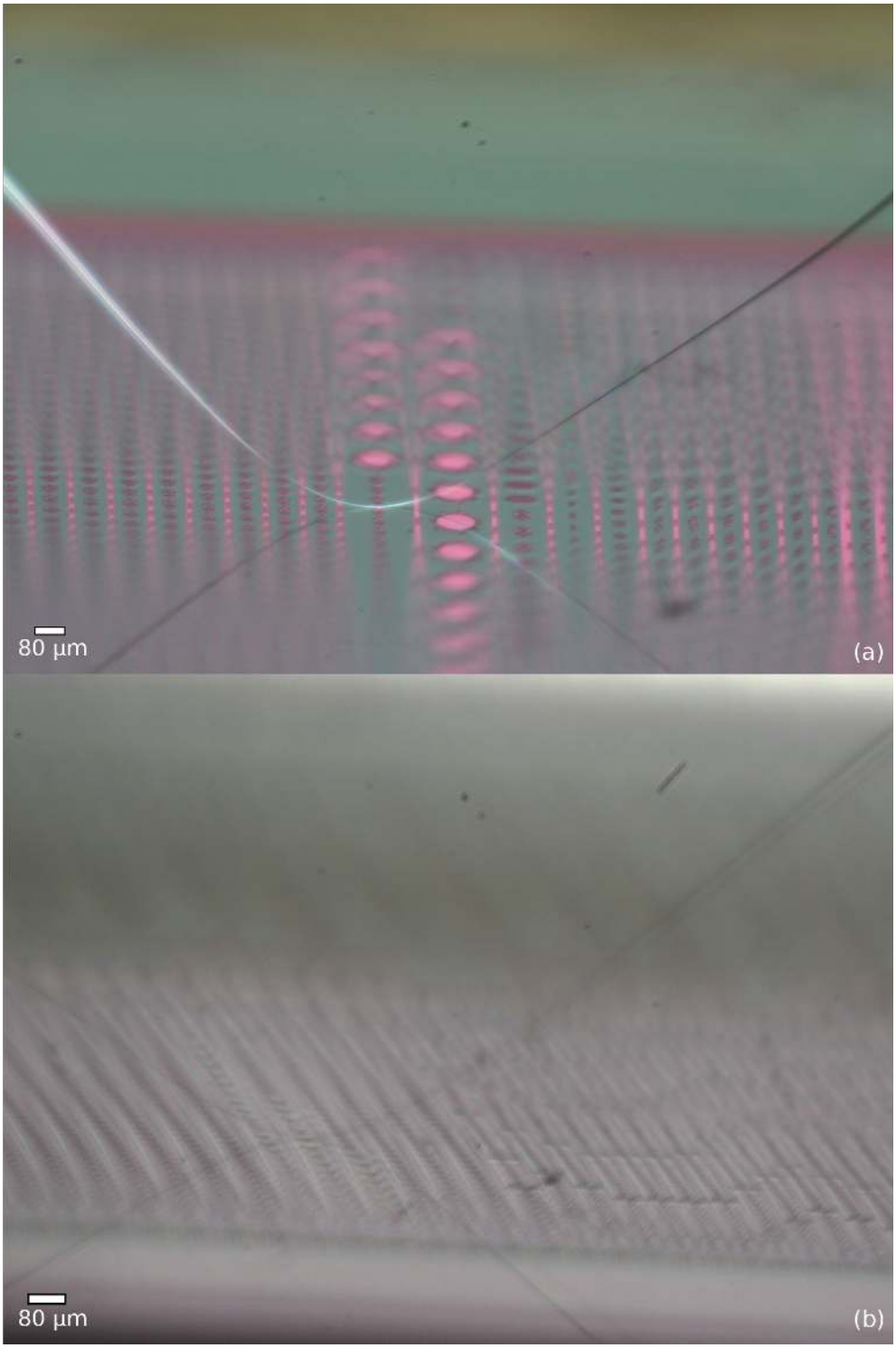

Figure 3.6: Pictures from the Questar telescope of the tapered fiber installed on the P-STM (a) outside of chamber, while attempting to couple to a 10 μm disc, and (b) in chamber, while coupling to a 38 μm diameter disc. The scale bars for each image were drawn to the scale of the resonators on chip.

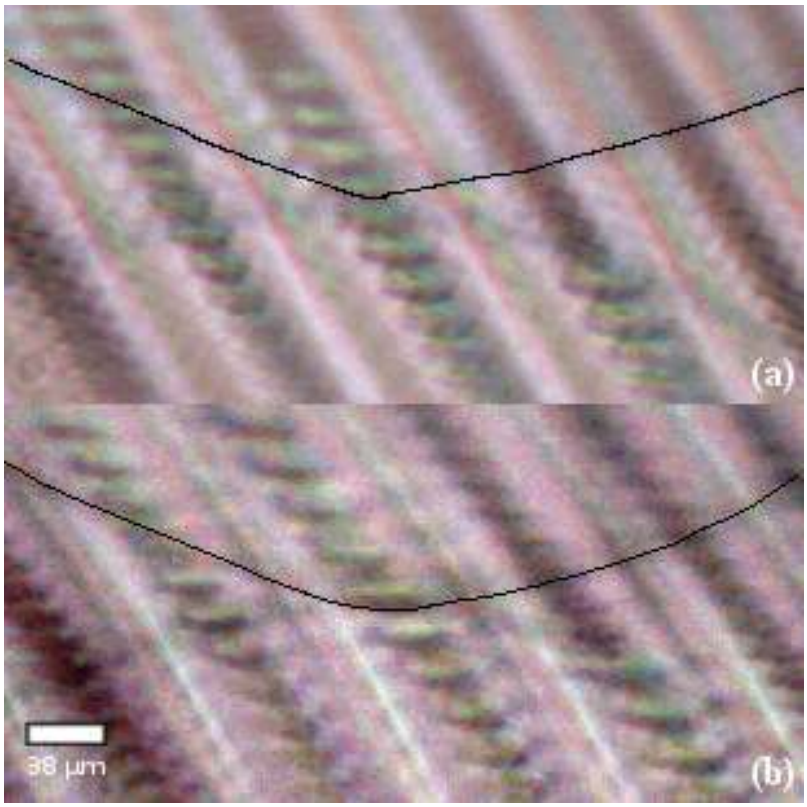

Figure 3.7: Cropped image of the fiber outlined in black when (a) above and (b) coupled to a 38 μm diameter disk in chamber. The scale bar applies to both images.

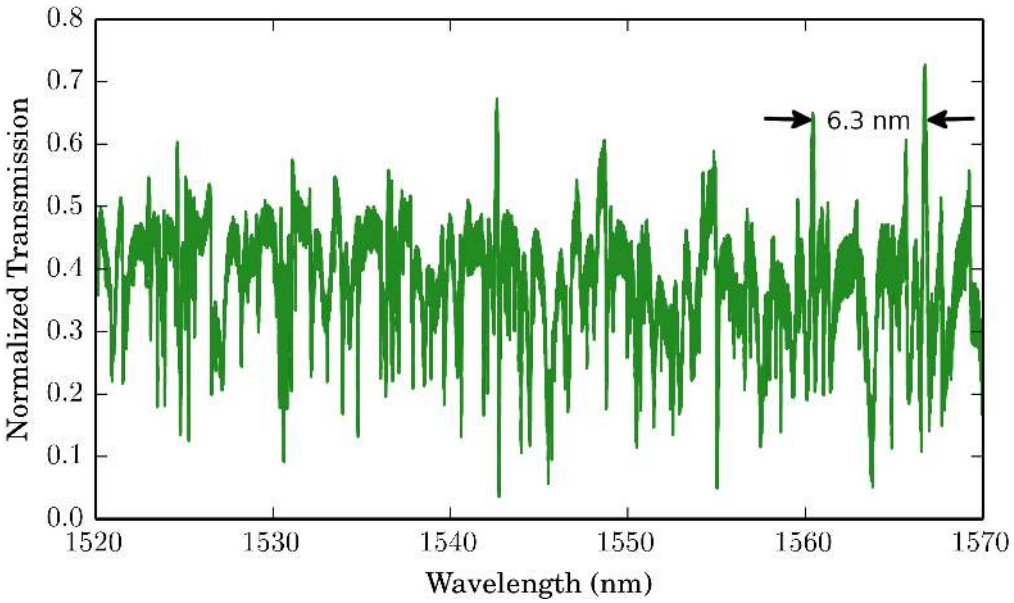

Figure 3.8: Normalized, repeating optical resonances of a 38 μm diameter disk. Free spectral range is 6.1 - 6.5 nm (750 - 800 GHz).

mechanical resonance is examined by a Zurich HF2LI lock-in amplifier by taking a fast Fourier transform (FFT) of the mechanical mode. Typically the settings for the FFT on the lock-in amplifier are a spectrum width of 230 kHz, a bandwidth of 2.5 to 10 kHz, and a sample rate of 230,000 samples/second gathering 4096 samples in total. The bandwidth was chosen to be on par with the relaxation time of the resonance, $Q_{\mathrm{mech},n}/(\Omega_n/2\pi)$. The lock-in was necessary since the spectrum analyzer could not analyze and sned the mechanical resonance data fast enough to the computer, which gave unreliable results upon further analysis. Other mechanical resonances can be seen using the same method.

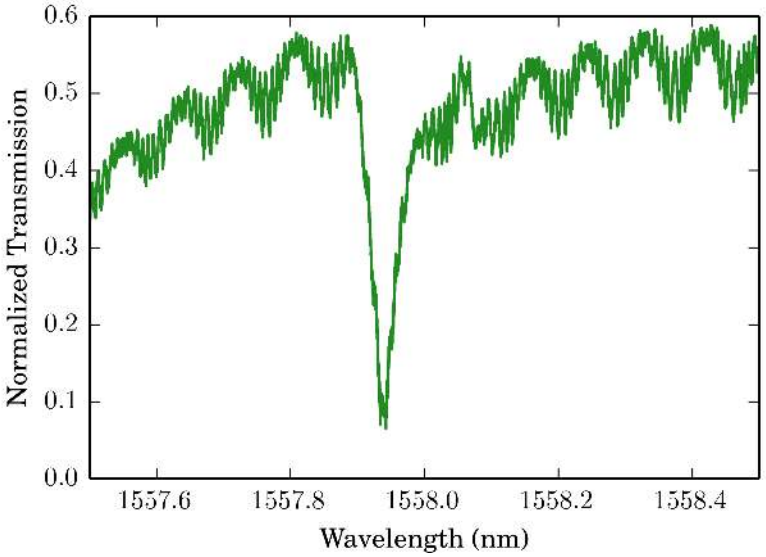

Figure 3.9: Normalized, high Q (45,000) optical resonance of a 38 μm diameter disk.

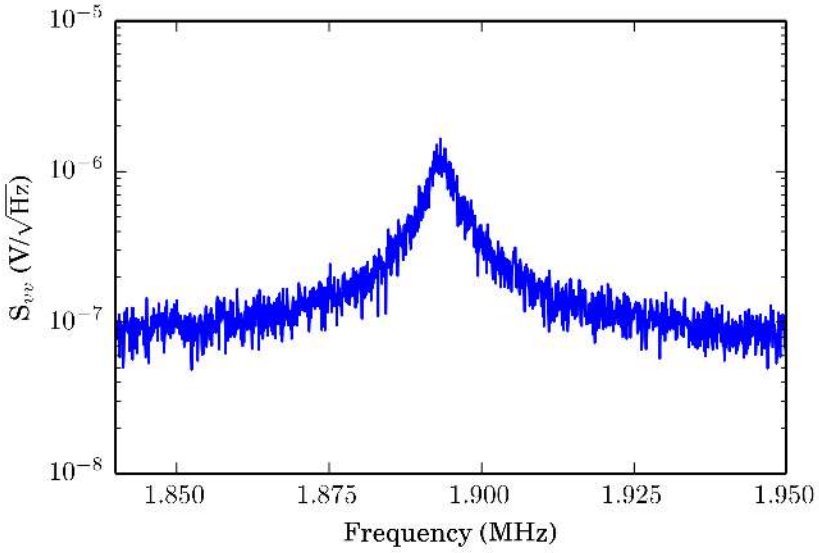

Figure 3.10: Thermomechanical power spectral density of the lower frequency mode in the 3.0 μm width flange torsional resonator from the lock-in amplifier, before calibration.

3.5 Difficulties Encountered

As mentioned before, the original Kapton wiring was completely replaced to overcome the lack of strain reliefs and improve reliability. At one point a LewVac vacuum optical feedthrough (FO-SM1300-16CF) broke, which was replaced by a custom built feedthrough. The new feedthrough was comprised of half a vacuum compatible optical patch cable which passed through both a PEEK tube and a 0.28 mm hole in a blank port. The end of the patch cable was glued using Epotek H77 to the PEEK tube and the cable itself was glued to the blank port. Strain relief has been somewhat of a problem with the PEEK tubing and will be replaced in the future by an aluminum one. Currently, the PEEK tubing is strain relieved by a clamp taped to the blank port of the feedthrough. The engineered optical feedthrough cost less than $50 for materials (as opposed to the market price of over $500 with a vacuum compatible optical patch cable) and is seen in Fig. 3.11.

3.5.1 Viewing Microdisks Inside the Vacuum Chamber

The viewing of microdisks disks through the Questar telescope was an obstacle throughout the experiment, especially when the P-STM was inside the chamber. After transporting the P-STM into the chamber, multiple reflections in the glass port between the telescope and the P-STM served to exacerbate this problem. The sharp side viewing angle (rather than a directly downward one), has hindered detailed viewing of smaller structures. The viewing area of the telescope when the sample is 22 cm away in the chamber is 2 mm in width by 1.5 mm in height with a depth of field of 40 μm. The resolution of Lumenera camera is 1616 x 1216 pixels yielding 2 μm per pixel, equivalent to the resolution of the telescope. The difference

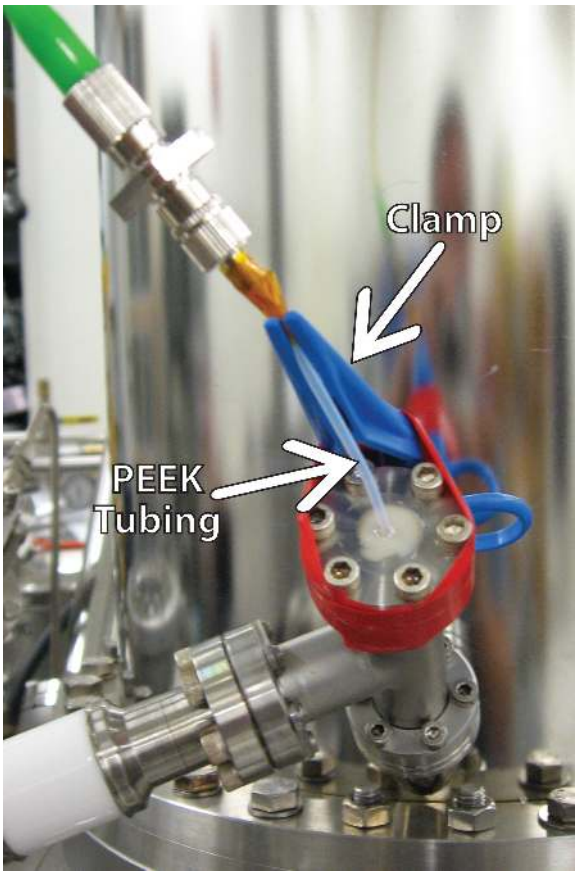

Figure 3.11: Custom built, vacuum compatible, optical feedthrough. A clamp taped to the blank port provides strain relief.

between viewing in air and viewing into the chamber through a glass port can be seen in Fig. 3.6 by the attempt to couple to a 10 μm disk in air and the lack of definition when viewing into the chamber (coupling to a 38 μm diameter disk). A cropped version of the fiber outlined when above and when coupling to a 38 μm diameter disk in chamber is seen in Fig. 3.7.

To add to this difficulty, in the future when radiation shields are attached around the P-STM for 4 K temperatures, lighting will be especially difficult using the telescope, since the current light is supplied from a glass port behind the P-STM, opposite of the telescope. The use of a camera to surmount this difficulty was proposed before, with the initial plan being to incorporate a NanEye 1 mm CCD camera, which would work in vacuum if the appropriate housing was built to hermetically seal it. For optimal viewing of the fiber atop a microdisk, the camera would be mounted on the P-STM head, between the fine piezo and the fiber holder, pointing in the downward direction, focused on the fiber. As a test for proof of concept, a 3rd Eye 520TVL FPV with a 9.5 mm CCD was bought, sealed in a custom aluminum housing, and attached to electrical feedthroughs in a vacuum chamber. It was proven to transmit clear images in a 10^{-3} mbar environment.

Next, an Awaiba NanEye GS camera with a CCD footprint of 3.4 mm x 3.4 mm was ordered which contained compound anti-reflection (AR) coated lenses. The NanEye GS was used for its substantially smaller CCD (3.4 mm), which would easily fit between the fine piezo and the fiber holder on the P-STM head, compared to the 3rd Eye 520TVL with a much larger CCD (9.5 mm).

The AR coating on the lenses was of an unknown composition and assumed to not be UHV compatible, therefore new achromatic lenses were ordered without the AR coating. The original design of a complex lens system was replaced by a single

aspherical lens which was encased in the original anodized aluminum housing, with a spacer to add extra focal distance. (The anodized coating can be removed later.) Another aluminum housing was made for the 3.4 mm CCD which threaded onto the lens housing. Both housings went through a three stage Epotek gluing and baking (110 °C) process, between which the camera was tested. The 3.4 mm CCD was wired to a custom printed ribbon cable, copper etched on Kapton film, with a PEEK intermediary connector, seen in Fig. 3.12. In the future, this ribbon cable will be useful for wiring the camera through the fine piezo in the P-STM head.

Figure 3.12: Vacuum compatible 3.4 mm CCD camera wired to a custom ribbon cable with a PEEK intermediary connector.

The focal distance between the lens and the CCD was evaluated with the help of David Fortin and following, images of on-chip structures were taken using the setup shown in Fig. 3.13, but progress was cut short. This stoppage was due to time constraints and obtaining of mechanical resonances taking a higher priority. An image of on-chip structures can be seen in Fig. 3.14 where the scale bar was obtained from the physical dimensions of the alignment pattern. The alignment pattern, seen as two "X"s on the top of Fig. 3.14, was made by deep UV etching, courtesy of Paul Kim. A camera will still be needed in the future to image smaller microdisks and allowing viewing when approaching cryogenic temperatures. The lighting for such

a camera will come from local ceramic LEDs, mounted to the posts securing the P-STM lower frame to the cryostat. Both the LEDs and the camera would be able to be turned off to obtain lower temperatures and a heat resistor placed inside the camera, in case lower temperatures raise the band gap energy enough to prevent the CCD from working properly [42].

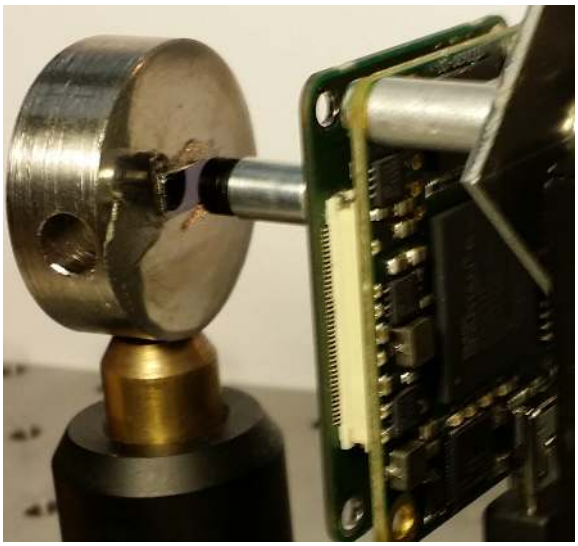

Figure 3.13: NanEye GS camera attached to USB controller board, examining a sample chip.

3.5.2 P-STM Scanning

Many problems appeared when the setup was attempted to scan optical resonators, using the optical scanning technique mentioned in Sec. 1.5. The major benefit of this method is that small, 10 μm disks might be able to be imaged, which could greatly ease fiber alignment when attempting to couple. A feedback loop using the optical transmission was attempted for constant optical current by changing the height of the taper relative to the sample through the center, fine piezo. One of the obstacles with this method is trying to align the scanning plane of the fiber parallel

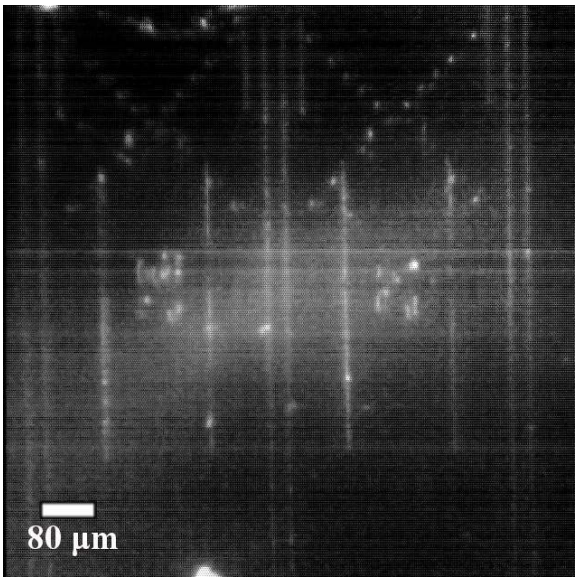

Figure 3.14: Image of on-chip structures taken with the NanEye GS camera using the setup in Fig. 3.13. Structures include an alignment pattern, along the top of the image, composed of two "X"s, created by deep UV etching. One of the alignment patterns can easily be seen in Fig. 3.15, for reference.

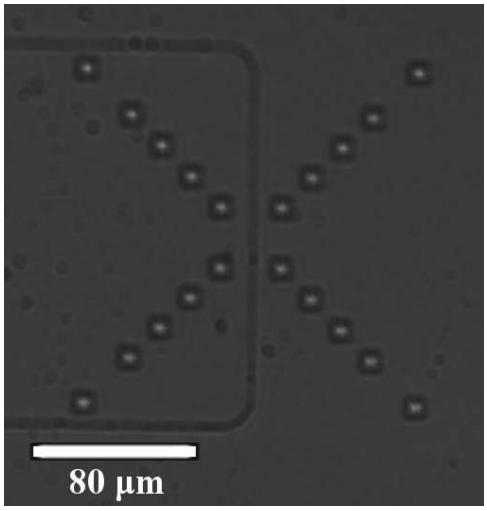

Figure 3.15: Image of on-chip structures taken with an optical microscope. An alignment pattern of one "X," created by deep UV etching, is clearly seen in the center. Both this and a second alignment pattern is seen in Fig. 3.14.

to the plane of the sample, since the tolerances are not high enough between the P-STM base, P-STM head disc, and the fine scanning piezo on the P-STM head. Plane subtraction is needed to account for this difference, which is done in software. The previous STM's fine scanning piezo was much shorter, having scanning areas of 100 x 100 nm at most. These smaller areas, as opposed to 25 x 25 μm areas scanned currently, did not require plane subtraction. While attempting to surmount this problem, the taper was scanned in constant height mode, with the topography image generated from the optical transmission. While optical topographies where generated, as seen in Fig. 3.16, on-chip structures were not able to be observed. The P-STM had to be extremely close to the sample, within one wavelength, in order for the optical transmission to be affected by the silicon device/handle layer. At these distances, stiction proved to be a major obstacle, meaning that when the taper was close enough to couple, the taper would be attracted electro-statically to the sample, where it would remain in contact during scanning. In the end, time was limited to spend on scanning and it was decided to couple to larger disks through visual alignment. Scanning using a constant optical transmission could still be possible, if more time was given to develop the software for plane subtraction.

David Fortin was a great contributer in introducing me to the P-STM, wiring, designing and machining various parts, assembling, LabView programming, and thinking of ways to couple optically. Fabrication of the sample and advice on coupling to optical resonators was possible with the help of Paul Kim. Joe Losby was of great help with the Zurich lock-in amplifier, etching samples, advice on vacuum systems and coupling, and relaying his vast knowledge of nanofabrication. Allison MacDonald and Hugh Ramp assisted in design of the optical circuit. Callum Doolin helped with some of the LabView setup as well. Thanks to Roshan and the Wolkow group

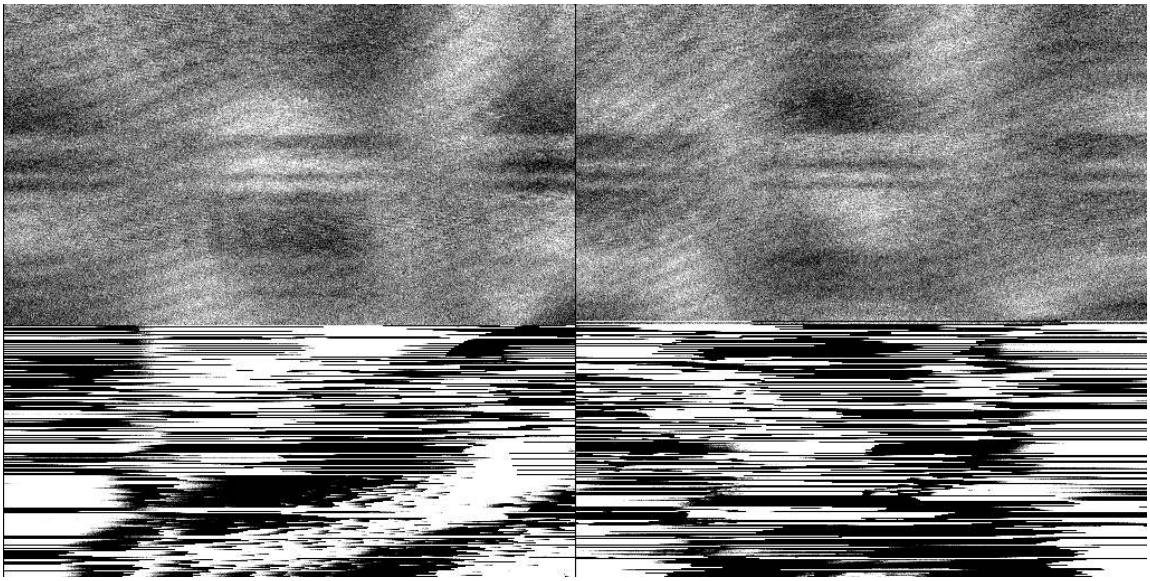

Figure 3.16: Scanned P-STM sample image obtained from changing optical transmission at constant height. Left side of the image is forward scanning left to right, while the right side of the image is backscanning right to left. Area scanned was 300 x 300 nm, scanned horizontally at 4.58 μm/s from top to bottom. On-chip structures were not able to be imaged. The tapered fiber started touching the sample during the lower half of the image and remained in contact for the duration, due to stiction.

for use of their optical microscope and camera.

Chapter 4

Results and Discussion

4.1 Optical Modes

After the fiber was positioned for optical coupling, the wavelength spectrum of the laser was scanned (1520 - 1570 nm) while recording the output transmission. Another optical scan was taken as well, that of the background spectrum when the fiber was well above the sample. The optical scan of the microdisk was normalized to this the background spectrum for each of the three 38 μm diameter discs and can be seen in Fig. 4.1. The wavelength spacing between the repeating optical modes in these scans, also known as the free spectral range, was 6.1 - 6.5 nm (750 - 800 GHz).

4.1.1 Fitting and Extracting Optical Properties

The optical spectrum was examined at modes which appeared to have a high Q. High Q modes are necessary to provide the greatest sensitivity to the nearby mechanics; the steeper the slope on the edge of an optical resonance, the greater change in transmission to the small optical AC signals caused by the nearby mechanics. These

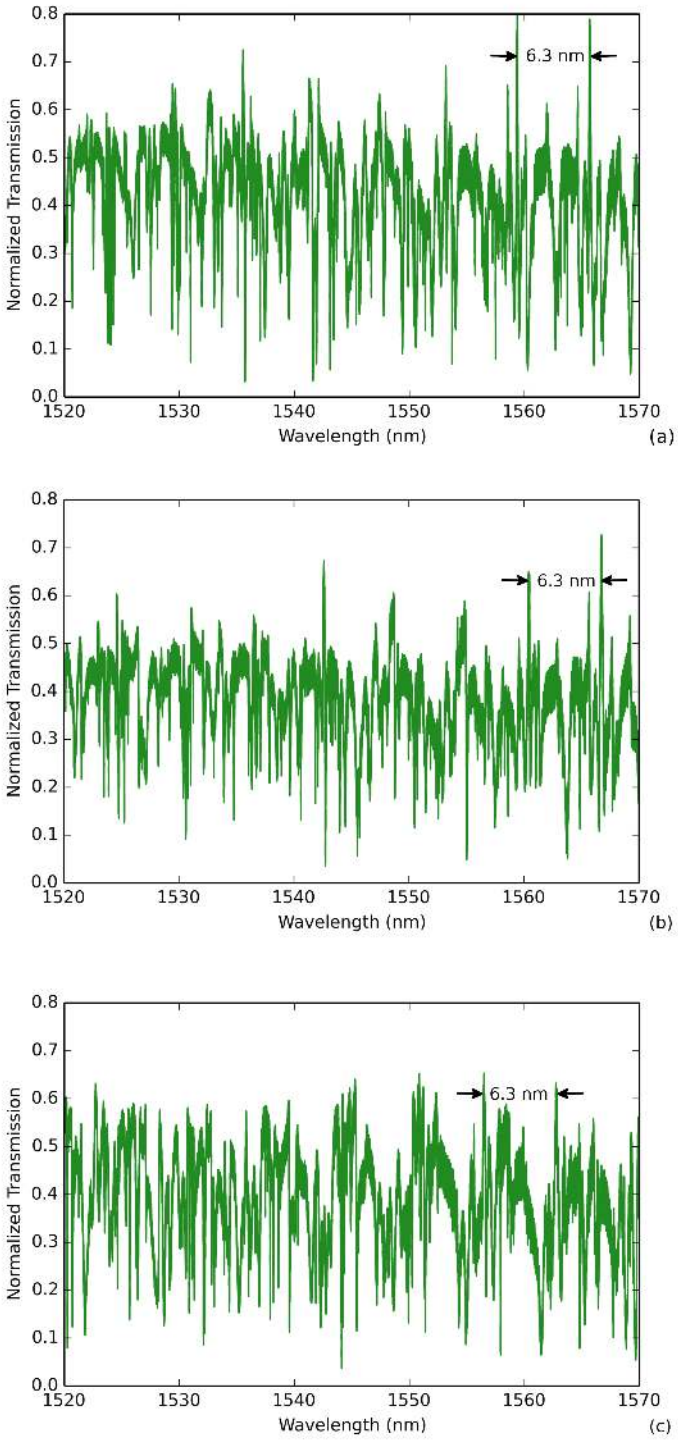

Figure 4.1: Optical resonances of the three 38 μm diameter microdisks adjacent to torsional resonators with flange widths of (a) 0.5 μm, (b) 1.5 μm, and (c) 3.0 μm. Each optical mode repeats throughout the spectrum and has a free spectral range of 6.1 - 6.5 nm (750 - 800 GHz).

high Q modes (without the off-resonance transmission) were fitted with Eq. 1.19, which was then used to find Q. The highest Q observed was 45,000 $\pm$ 700 with a κ of 4.26 GHz. This optical mode can be seen in Fig. 4.2. The high frequency oscillations, seen off resonance, is from optical interference, possibly from a less than ideal optical splice, the taper itself, or other sources.

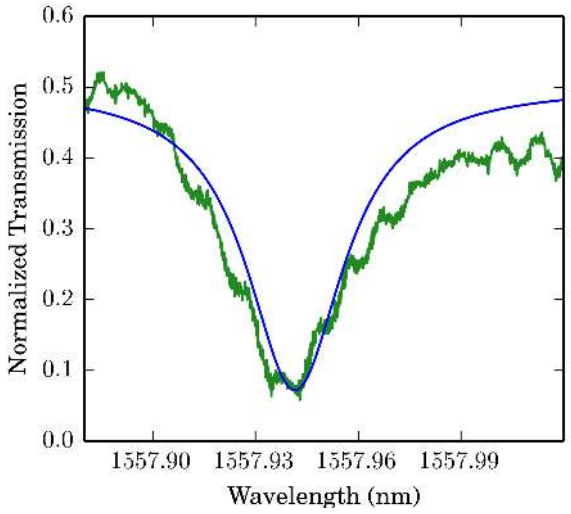

Figure 4.2: Highest Q optical resonance observed (green) with best fit (blue) from Eq. 1.19, having a Q of 45,000. The high frequency oscillations, seen off resonance, could be from a less than ideal optical splice, the taper itself, or other sources.

4.2 Mechanical Modes

The mechanical spectrum was detected with a spectrum analyzer with the laser detuned to the side of one of the resonances similar to Fig. 4.2. During this sampling, the chamber was pumped down already with the sample in the 10^{-7} mbar environment. Two mechanical resonances were seen in each mechanical device, with the exception of the 0.5 μm width flange having only one. These resonances were from thermomechanical motion and are seen in Fig. 4.3.

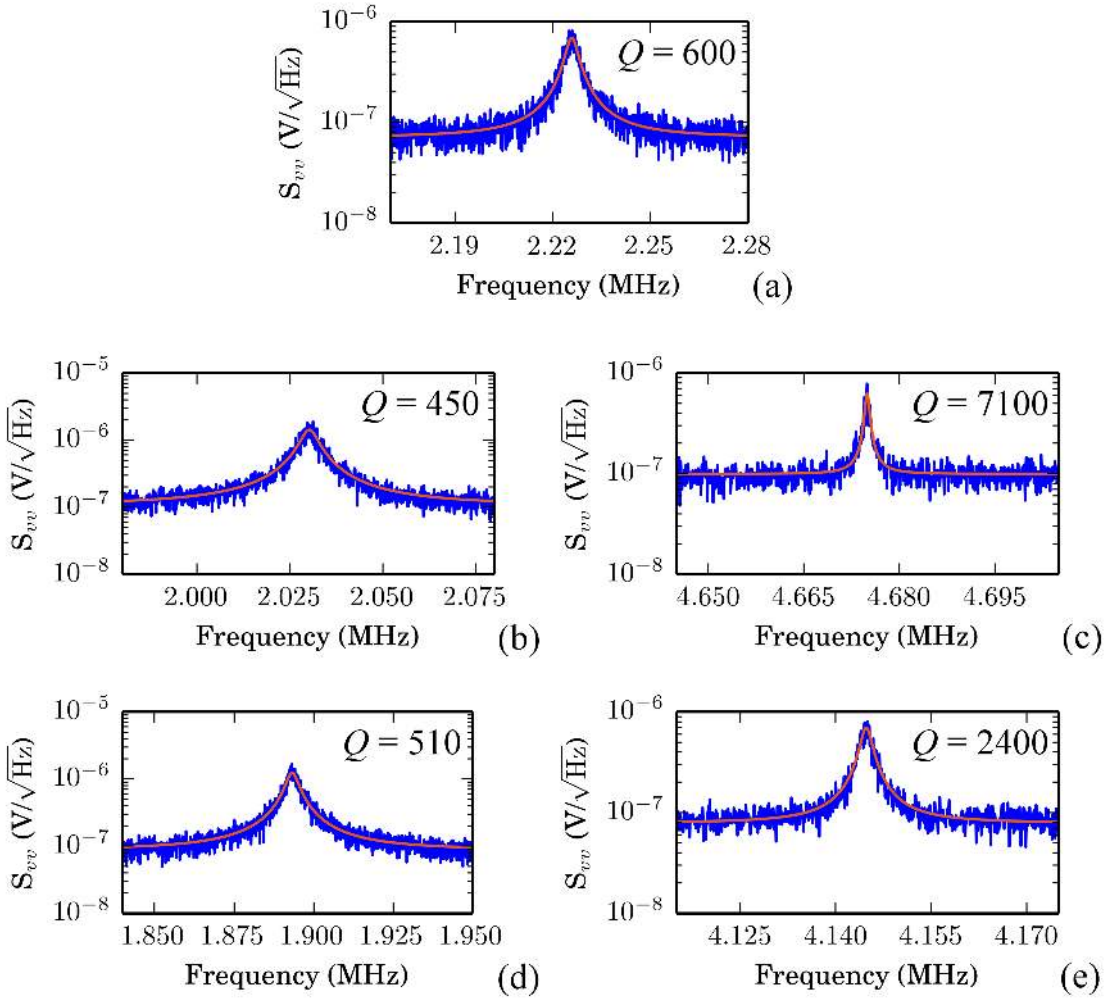

Figure 4.3: Mechanical resonances plotted with the data in blue and the fits in red. Flange widths and frequencies of (a) 0.5 μm and 2.23 MHz, (b) 1.5 μm and 2.03 MHz, (c) 1.5 μm and 4.68 MHz, (d) 3.0 μm and 1.89 MHz, and (e) 3.0 μm and 4.14 MHz.

All of the resonators have a lower frequency mode (1.8 - 2.2 MHz) which is the largest in amplitude out of the two possible resonances in each device. This is to be expected since the lower mode is certainly a torsional mode, which is more easily stimulated since the resonators are torsional. A wider flange increases the mass of the resonator with the moment of inertia for the torsional mode, which in turn lowers the frequency of both the higher and lower modes. Another point of interest is the higher frequency mode in the 0.5 μm width flange was not seen. This is most likely from the mode having less magnitude than that of the electrical system's noise floor.

Mechanical resonances were not able to be seen at higher pressures due to the tapered fiber loosing coupling with the microdisk when the pumps were turned off. During coupling, the both the turbo and scroll pump were on. After coupling, the pumps were turned off which caused the tapered fiber to loose contact (and coupling as well) with the microdisk. The reason for the change is the fiber was adjusted to sit on the sample when the pumps were turned on, but when the pumps were turned off, the calibration distance between the P-STM and the sample changed slightly. This slight change is distance was enough for the fiber to loose contact with the microdisk it was coupling to. Even though coupling at a lower vacuum was not attained, it can be hypothesized that at high pressures, the mechanical quality factor should decrease along with the amplitude of the peak [17].

4.3 Simulated Mechanical Modes

In order to compare the experimental results to the simulations, finite element modeling (FEM) using COMSOL was performed on each of the three mechanical resonators, using a template provided by Paul Kim and dimensions obtained from a

SEM. The three lowest frequencies and mode shapes are seen in Fig. 4.4.

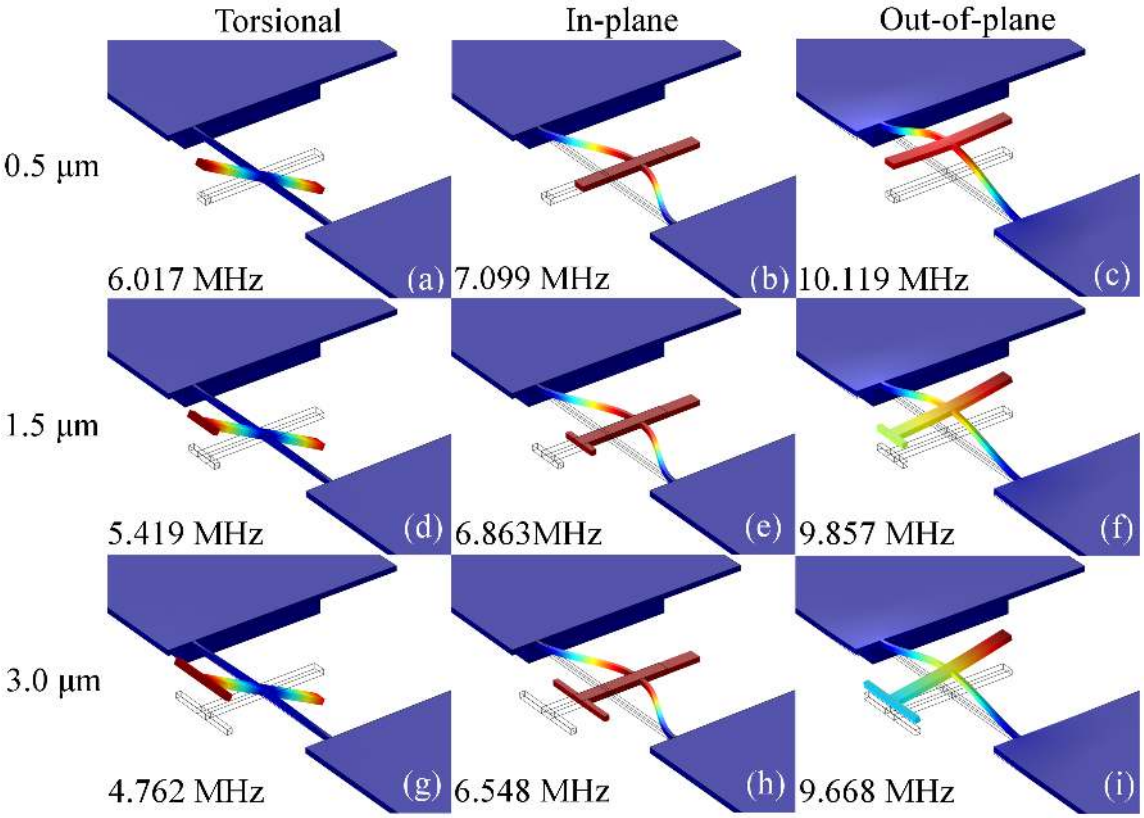

Figure 4.4: FEM simulations of the mechanical modes in torsional resonators with flange widths of (a) 0.5 μm, torsional mode, with frequency 6.017 MHz; (b) 0.5 μm, in-plane mode, with frequency 7.099 MHz; (c) 0.5 μm, out-of-plane mode, with frequency 10.119 MHz; (d) 1.5 μm, torsional mode, with frequency 5.419 MHz; (e) 1.5 μm, in-plane mode, with frequency 6.863 MHz; (f) 1.5 μm, out-of-plane mode, with frequency 10.119 MHz; (g) 3.0 μm, torsional mode, with frequency 4.762 MHz; (h) 3.0 μm, in-plane mode, with frequency 6.548 MHz; and (i) 3.0 μm, out-of-plane mode, with frequency 9.668 MHz.

While the resonant frequencies of the FEM simulations deviate greatly from the experimental results, conclusions may still be drawn between them. The inverse relationship between flange width and the fundamental torsional mode frequency still exists in the simulations. Given the approximately the same optomechanical coupling for both modes, it makes sense that the lowest frequency mode has the

highest amplitude since it is the most easily excited. Assuming relatively the same optomechanical coupling for each mode and that the easiest thermomechanically stimulated mode would be a torsional one, it is fair to state that the lower frequency mode seen in each device is a torsional mode. The higher frequency mode, is probably the in-plane mode, not only since it is the next mode in higher frequency, but the next higher frequency modes are much greater in frequency (∼6 compared to ∼9 MHz). These deviations of the experiment from the simulations are probably from the difference in the fabricated device compared to the computerized ideal (e.g. from undercutting, slanted sidewalls, SEM has resolution down to 10 nm).

4.4 Thermomechanical Calibration

The mechanical resonances were fitted using Eq. 1.45, as described in Sec. 1.4. The fits can be seen in Fig. 4.3 with the extracted mechanical properties in Table 4.1 and the angular properties in Table 4.2 (the angular properties are only listed for the torsional modes). It should be noted that since the simulated modal frequency (Ω_n^{sim}) is at most 2.5 times greater than the experimental modal frequency (Ω_n^{exp}), it is possible that the effective mass is at most 6.35 times greater than the values listed in the below tables. COMSOL calculated the simulated modal frequency from both the effective mass and the effective spring constant, $\Omega_n^{\text{sim}} = \sqrt{k_{\text{eff}}/m_{\text{eff}}}$ which means that the effective mass, the effective spring constant, or both, may be off by a factor as great as 6.35.

The optomechanical coupling coefficient, G, was found using the methodology at the end of Sec. 1.4, where the side of the optical resonance, at which the mechanical data was obtained, was linearly fitted and the slope extracted. This was combined

Table 4.1: Calibrated Properties of the Torsional Resonators

Flange Width (μm)	m_{eff} (fg)	$\Omega_n^{\text{exp}}/2\pi$ (MHz)	$\Omega_n^{\text{sim}}/2\pi$ (MHz)	Q_{mech}	$\sqrt{S_{zz}^{\text{nf}}}$ (fm Hz$^{-1/2}$)
0.5	420	2.23	6.02	600 ± 8	300 ± 20
1.5	1500	4.68	6.86	7100 ± 200	280 ± 7
1.5	490	2.03	5.42	450 ± 5	200 ± 10
3.0	1700	4.14	6.55	2400 ± 50	220 ± 10
3.0	610	1.89	4.76	510 ± 5	200 ± 10

Table 4.2: Calibrated Angular Properties of the Torsional Resonators

Flange Width (μm)	I_{eff} (μm^2 pg)	$\Omega_n^{\text{exp}}/2\pi$ (MHz)	$\Omega_n^{\text{sim}}/2\pi$ (MHz)	$\sqrt{S_{\theta\theta}^{\text{nf}}}$ (nrad Hz$^{-1/2}$)
0.5	2.6	2.23	6.02	120 ± 6
1.5	3.0	2.03	5.42	81 ± 5
3.0	3.8	1.89	4.76	80 ± 5

with the conversion factor, α, and the 4x amplification of AC output inherent of the New Focus 1811 Photoreceiver accounted for, as seen in Eq. 1.49. The zero point fluctuation amplitude, x_{zpf}, was found using Eq. 1.51. This value was then used to calculate the single photon/phonon coupling rate, g_0, through Eq. 1.50. The values of the optomechanical coupling coefficient are seen in Table 4.3.

As expected, x_{zpf} scaled with device mass and resonant frequency. The optomechanical coupling coefficient, $G/2\pi$ was greatest for the larger flange widths since the longer edge allowed for greater optical mode overlap. This trend is reflected in g_0 as

Table 4.3: Optomechanical coupling properties

Flange Width (μm)	$\Omega_n^{\text{exp}}/2\pi$ (MHz)	$\Omega_n^{\text{sim}}/2\pi$ (MHz)	x_{zpf} (fm)	$G/2\pi$ (MHz/nm)	g_0 (Hz)
0.5	2.23	6.02	95 ± 0.6	0.82 ± 0.02	78 ± 2
1.5	4.68	6.86	35 ± 0.6	1.8 ± 0.05	63 ± 2
1.5	2.03	5.42	92 ± 0.5	2.7 ± 0.07	250 ± 6
3.0	4.14	6.55	58 ± 0.2	69 ± 2	4000 ± 10
3.0	1.89	4.76	85 ± 0.3	82 ± 3	7000 ± 200

well. In comparison, a different mechanical resonator design with a flange width of 1.5 μm and an optical microdisk diameter of 10 μm, gave $G/2\pi$ to be 82 MHz/nm, similar to that of the torsional mode in the 3.0 μm width flange, seen here [18]. While the 3.0 μm flange width devices should have greater coupling than the 1.5 μm ones, the 38 μm diameter optical disks, investigated here, a smaller disk could perhaps give greater coupling from increased optical mode overlap.

Callum Doolin provided great assistance in fitting and troubleshooting the data, especially in determining the optomechanical coupling coefficient. Bradley Hauer's help was greatly appreciated in fitting and extracting all parameters.

Chapter 5

Conclusion

5.1 Summary and Directions for Future Work

Using an existing STM, a P-STM was built which required augmenting the existing STM with an entirely new head, enhancing the sample holder, and completely rewiring the setup. In order to couple to optical resonators, a new fiber holder was engineered and a tapered fiber pulled and mounted, necessitating changes to the current fiber pulling setup. Following installation of the tapered fiber onto the P-STM and transferring the P-STM to a HV (10^{-7} mbar) environment, coupling was accomplished to multiple microdisks of 38 μm in diameter where optical quality factors as high as 45,000 $\pm$ 700 were seen. The optical modes of the microdisks were able to couple to each of the adjacent torsional resonators, through which up to two mechanical modes per resonator were discerned. Following a thermomechanical calibration of each resonance, sensitivities as low as 200 $\pm$ 10 (fm $\text{Hz}^{-1/2}$) and Q_{mech} as high as 7,100 $\pm$ 200 were observed on different resonances. Angular sensitivities as low as 80 $\pm$ 5 (nrad $\text{Hz}^{-1/2}$) were observed as well. FEM simulations of the torsional resonators

helped identify which modes were seen and suggest that the lower frequency modes are torsional whereas the higher modes are in-plane. Optomechanical coupling as high as 82 ± 3 MHz/nm was observed as well as a zero point motion of 35 ± 0.6 fm was inferred on other devices.

While the setup was successful in observing mechanical modes, many improvements can be made. Coupling to smaller resonators was difficult given the optical alignment of the fiber to the microdisk requiring viewing with a telescope through a glass port, where multiple reflections inhibited detailed viewing. Scanning of the optical topography was limited since the taper was required to be within one wavelength of the sample, maintaining a constant optical transmission by adjusting the height of the taper through the center, fine piezo. This would allow mapping the surface of the sample from the shifts in height of the taper, and would potentially allow coupling to 10 μm disks, which might yield greater optomechanical coupling. Stiction and changes in the software for plane subtraction required more time than was currently available, but scanning remains a future possibility. Another possible improvement is installing a camera directly above the tapered fiber, between the fiber holder and the fine, center piezo. The camera, together with local ceramic LEDs, would make viewing of the sample possible when the radiation shields are attached in the future, for liquid helium temperatures.

UHV is possible (10^{-11} mbar) if the apparatus was baked-out and any leaks in the chamber sealed. A UHV environment will be better at not only keeping a sample clean long term, but has the possibility of performing electronic beam, molecular, or atomic deposition. Liquid He temperatures are also possible, but since a shield is required around the P-STM in order to do so, new lighting must be made available using local ceramic LEDs. Different optical and mechanical resonators

could be investigated including a torsional resonator with magnetic permalloy thin-film deposited on one of its paddles. This would not only posses the ability for remote actuation, but can also be used as a highly sensitive mechanical platform for magnetic state manipulation. This actuation and manipulation would be accomplished by applying a variable magnetic field beneath the sample with a dither coil, measured with a Hall Probe, and using a static field through a magnet placed in chamber moved with an already present arm.

In short, not only were mechanical resonances observed with high sensitivity, but the P-STM holds a great amount of future possibilities.

Bibliography

[1] H. Cavendish, "Experiments to Determine the Density of the Earth. By Henry Cavendish, Esq. F. R. S. and A. S.," *Philosophical Transactions of the Royal Society of London* **88** (1798) 469–526, http://rstl.royalsocietypublishing.org/content/88/469.full.pdf.

[2] G. G. Luther and W. R. Towler, "Redetermination of the Newtonian Gravitational Constant G," *Phys. Rev. Lett.* **48** (Jan, 1982) 121–123. http://link.aps.org/doi/10.1103/PhysRevLett.48.121.

[3] A. Cleland and M. Roukes, "A nanometre-scale mechanical electrometer," *Nature* **392** (1998) 160–162. http://dx.doi.org/10.1038/32373.

[4] J. P. Davis, D. Vick, J. A. J. Burgess, D. C. Fortin, P. Li, V. Sauer, W. K. Hiebert, and M. R. Freeman, "Observation of magnetic supercooling of the transition to the vortex state," *New Journal of Physics* **12** (2010) 093033. http://stacks.iop.org/1367-2630/12/i=9/a=093033.

[5] H. B. Chan, V. A. Aksyuk, R. N. Kleiman, D. J. Bishop, and F. Capasso, "Quantum Mechanical Actuation of Microelectromechanical Systems by the Casimir Force," *Science* **291** (2001) 1941–1944, http://www.sciencemag.org/content/291/5510/1941.full.pdf.

[6] J. H. Condon and J. A. Marcus, "Fermi Surface of Calcium by the de Haas-van Alphen Effect," *Phys. Rev.* **134** (Apr, 1964) A446–A452. http://link.aps.org/doi/10.1103/PhysRev.134.A446.

[7] C. Lupien, B. Ellman, P. Grtter, and L. Taillefer, "Piezoresistive torque magnetometry below 1 K," *Applied Physics Letters* **74** (1999) .

[8] R. N. Kleiman, G. K. Kaminsky, J. D. Reppy, R. Pindak, and D. J. Bishop, "Single-crystal silicon high-Q torsional oscillators," *Review of Scientific Instruments* **56** (1985) .

[9] D. J. Bishop and J. D. Reppy, "Study of the superfluid transition in two-dimensional ^{4}He films," *Phys. Rev. B* **22** (Dec, 1980) 5171–5185. http://link.aps.org/doi/10.1103/PhysRevB.22.5171.

[10] D. E. Farrell, C. M. Williams, S. A. Wolf, N. P. Bansal, and V. G. Kogan, "Experimental Evidence for a Transverse Magnetization of the Abrikosov Lattice in Anisotropic Superconductors," *Phys. Rev. Lett.* **61** (Dec, 1988) 2805–2808. http://link.aps.org/doi/10.1103/PhysRevLett.61.2805.

[11] A. C. Bleszynski-Jayich, W. E. Shanks, B. Peaudecerf, E. Ginossar, F. von Oppen, L. Glazman, and J. G. E. Harris, "Persistent Currents in Normal Metal Rings," *Science* **326** (2009) 272–275, http://www.sciencemag.org/content/326/5950/272.full.pdf.

[12] R. A. Beth, "Mechanical Detection and Measurement of the Angular Momentum of Light," *Phys. Rev.* **50** (Jul, 1936) 115–125. http://link.aps.org/doi/10.1103/PhysRev.50.115.

[13] J. A. J. Burgess, A. E. Fraser, F. F. Sani, D. Vick, B. D. Hauer, J. P. Davis, and M. R. Freeman, "Quantitative Magneto-Mechanical Detection and Control of the Barkhausen Effect," *Science* **339** (2013) 1051–1054, http://www.sciencemag.org/content/339/6123/1051.full.pdf.

[14] G. S. Wiederhecker, L. Chen, A. Gondarenko, and M. Lipson, "Controlling photonic structures using optical forces," *Nature* **462** (2009) 633–636. http://dx.doi.org/10.1038/nature08584.

[15] K. Srinivasan, H. Miao, M. T. Rakher, M. Davanco, and V. Aksyuk, "Optomechanical Transduction of an Integrated Silicon Cantilever Probe Using a Microdisk Resonator," *Nano Letters* **11** (2011) 791–797. http://pubs.acs.org/doi/abs/10.1021/nl104018r.

[16] A. G. Krause, M. Winger, T. D. Blasius, Q. Lin, and O. Painter, "A high-resolution microchip optomechanical accelerometer," *Nat Photon* **6** (2012) 768–772. http://dx.doi.org/10.1038/nphoton.2012.245.

[17] P. H. Kim, C. Doolin, B. D. Hauer, A. J. R. MacDonald, M. R. Freeman, P. E. Barclay, and J. P. Davis, "Nanoscale torsional optomechanics," *Applied Physics Letters* **102** (2013) . http://scitation.aip.org/content/aip/journal/apl/102/5/10.1063/1.4789442.

[18] P. H.-C. Kim, *Nanoscale Torsional Optomechanics*. PhD thesis, University of Alberta, 2014.

[19] T. J. Kippenberg and K. J. Vahala, "Cavity Opto-Mechanics," *Opt. Express* **15** (Dec, 2007) 17172–17205. http://www.opticsexpress.org/abstract.cfm?URI=oe-15-25-17172.

[20] B. P. Abbott, R. Abbott, R. Adhikari, P. Ajith, B. Allen, G. Allen, R. S. Amin, S. B. Anderson, W. G. Anderson, *et al.*, "LIGO: the Laser Interferometer Gravitational-Wave Observatory," *Reports on Progress in Physics* **72** (2009) 076901. http://stacks.iop.org/0034-4885/72/i=7/a=076901.

[21] M. Aspelmeyer, T. J. Kippenberg, and F. Marquardt, "Cavity Optomechanics," *ArXiv e-prints* (2013) , arXiv:1303.0733 [cond-mat.mes-hall].

[22] V. Giovannetti, S. Lloyd, and L. Maccone, "Quantum-Enhanced Measurements: Beating the Standard Quantum Limit," *Science* **306** (2004) 1330–1336, http://www.sciencemag.org/content/306/5700/1330.full.pdf. http://www.sciencemag.org/content/306/5700/1330.abstract.

[23] J. Aasij, J. Abadiej, *et al.*, "Enhanced sensitivity of the LIGO gravitational wave detector by using squeezed states of light," *Nat Photon* **7** (2013) 613–619. http://dx.doi.org/10.1038/nphoton.2013.177.

[24] M. Eichenfield, R. Camacho, J. Chan, K. J. Vahala, and O. Painter, "A picogram- and nanometre-scale photonic-crystal optomechanical cavity," *Nature* **459** (2009) 550–555. http://dx.doi.org/10.1038/nature08061.

[25] C. Doolin, P. H. Kim, B. D. Hauer, A. J. R. MacDonald, and J. P. Davis, "Multidimensional optomechanical cantilevers for high-frequency force sensing," *New Journal of Physics* **16** (2014) 035001. http://stacks.iop.org/1367-2630/16/i=3/a=035001.

[26] C. V. Raman and G. A. Sutherland, "On the Whispering-Gallery Phenomenon," *Proceedings of the Royal Society of London A: Mathematical, Physical and Engineering Sciences* **100** (1922) 424–428.

[27] Safavi, S. Groblacher, J. T. Hill, J. Chan, M. Aspelmeyer, and O. Painter, "Squeezed light from a silicon micromechanical resonator," *Nature* **500** (2013) 185–189. http://dx.doi.org/10.1038/nature12307.

[28] L. He, S. K. Ozdemir, and L. Yang, "Whispering gallery microcavity lasers," *Laser Photonics Reviews* **7** (2013) 60–82. http://dx.doi.org/10.1002/lpor.201100032.

[29] B. Li, X.-F. Jiang, Q. Gong, and Y.-F. Xiao, "Raman laser from an on chip, high Q polymer microcavity," in *CLEO: 2013*, p. JW2A.39. Optical Society of America, 2013. http://www.opticsinfobase.org/abstract.cfm?URI=CLEO_AT-2013-JW2A.39.

[30] C. Regal, J. Teufel, and K. Lehnert, "Measuring nanomechanical motion with a microwave cavity interferometer," *Nat Phys* **4** (2008) 555–560. http://dx.doi.org/10.1038/nphys974.

[31] M. Eichenfield, J. Chan, A. H. Safavi-Naeini, K. J. Vahala, and O. Painter, "Modeling dispersive coupling and losses of localized optical andmechanical modes in optomechanicalcrystals," *Opt. Express* **17** (2009) 20078–20098. http://www.opticsexpress.org/abstract.cfm?URI=oe-17-22-20078.

[32] G. Anetsberger, *Novel Cavity Optomechanical Systems at the Micro- and Nanoscale and Quantum Measurements of Nanomechanical Oscillators*. PhD thesis, Ludwig Maximilian University of Munich, 2010.

[33] C. Doolin, B. D. Hauer, P. H. Kim, A. J. R. MacDonald, H. Ramp, and J. P. Davis, "Nonlinear optomechanics in the stationary regime," *Phys. Rev. A* **89** (May, 2014) 053838. http://link.aps.org/doi/10.1103/PhysRevA.89.053838.

[34] B. Hauer, C. Doolin, K. Beach, and J. Davis, "A general procedure for thermomechanical calibration of nano/micro-mechanical resonators," *Annals of Physics* **339** (2013) 181 – 207. http://www.sciencedirect.com/science/article/pii/S0003491613001723.

[35] H. R. G. Binnig, "Scanning tunneling microscopy," *Helvetica Physica Acta* **55** (1982) 726.

[36] M. Eichenfield, C. P. Michael, R. Perahia, and O. Painter, "Actuation of micro-optomechanical systems via cavity-enhanced optical dipole forces," *Nat Photon* **1** (2007) 416–422. http://dx.doi.org/10.1038/nphoton.2007.96.

[37] B. Hauer, P. Kim, C. Doolin, A. MacDonald, H. Ramp, and J. Davis, "On-chip cavity optomechanical coupling," *EPJ Techniques and Instrumentation* **1** (2014) 4. http://www.epjtechniquesandinstrumentation.com/content/1/1/4.

[38] M. Borselli, *High-Q microresonators as lasing elements for silicon photonics*. PhD thesis, California Institute of Technology, May, 2006.

[39] J. M. Ward, D. G. OShea, B. J. Shortt, M. J. Morrissey, K. Deasy, and S. G. Nic Chormaic, "Heat-and-pull rig for fiber taper fabrication," *Review of Scientific Instruments* **77** (2006) . http://scitation.aip.org/content/aip/journal/rsi/77/8/10.1063/1.2239033.

[40] G. Kakarantzas, T. E. Dimmick, T. A. Birks, R. L. Roux, and P. S. J. Russell, "Miniature all-fiber devices based on CO2 laser microstructuring of tapered fibers," *Opt. Lett.* **26** (Aug, 2001) 1137–1139. http://ol.osa.org/abstract.cfm?URI=ol-26-15-1137.

[41] S. Harun, K. Lim, C. Tio, K. Dimyati, and H. Ahmad, "Theoretical analysis and fabrication of tapered fiber," *Optik - International Journal for Light and Electron Optics* **124** (2013) 538 – 543. http://www.sciencedirect.com/science/article/pii/S0030402612000654.

[42] W. Bludau, A. Onton, and W. Heinke, "Temperature dependence of the band gap of silicon," *Journal of Applied Physics* **45** (1974) .